

Imaging of the electrical activity in the root zone under limited water availability stress: A laboratory study for *Vitis vinifera*.

Benjamin Mary^{1,2}, Veronika Iván¹, Franco Meggio^{3,4}, Luca Peruzzo^{1,2}, Guillaume Blanchy⁵, Chunwei Chou², Benedetto Ruperti^{3,4}, Yuxin Wu², Giorgio Cassiani¹

¹Dipartimento di Geoscienze, Università degli Studi di Padova, Padova, Italy

²Earth and Environmental Sciences Area, Lawrence Berkeley National Laboratory, California, USA

³Department of Agronomy, Food, Natural resources, Animals and Environment – DAFNAE, University of Padova, Agripolis, Viale dell'Università 16 – Legnaro (Padova), Italy;

⁴Interdepartmental Research Centre for Viticulture and Enology - CIRVE, University of Padova, Via XXVIII Aprile 14, Conegliano (Treviso), Italy;

⁵Urban and Environmental Engineering, University of Liège (ULiege), Liège, Belgium

Correspondence to: B. Mary (benjamin.mary@unipd.it)

Abstract

Understanding root signals and their consequences on the whole plant physiology is one of the keys to tackling the water-saving challenge in agriculture. The implementation of water-saving irrigation strategies, such as the partial root-zone drying (PRD) method, as part of a comprehensive approach to enhance water use efficiency. To reach this goal tools are needed for the evaluation of the root's and soil water dynamics in time and space. In controlled laboratory conditions, using a rhizotron built for geoelectrical tomography imaging, we monitored the spatio-temporal changes in soil electrical resistivity (ER) for more than a month corresponding to 8 alternating water inputs cycles. Electrical Resistivity Tomography (ERT) was complemented with Electrical Current Imaging (ECI) using plant stem-induced electrical stimulation. To estimate soil water content in the rhizotron during the experiment, we incorporated Archie's law as a constitutive model. We demonstrated that under mild water stress conditions, it is practically impossible to spatially distinguish the limited water availability effects using ECI. We evidenced that the Current Source Density spatial distribution varied during the course of the experiment with

4

25 the transpiration demand but without any significant relationship to the soil water content changes . On the other hand, ERT
26 showed spatial patterns associated with irrigation and, to a lesser degree, to RWU and hydraulic redistribution. The
27 interpretation of the geoelectrical imaging with respect to root activity was strengthened and correlated with indirect
28 observations of the plant transpiration using a weight monitoring lysimeter and direct observation of the plant leaf gas
29 exchanges.

30 1. Introduction

31 In the context of water scarcity, agriculture needs to improve irrigation practices by reducing water inputs and selecting
32 adequate species and, in the case of woody crops, most efficient scion-rootstock combinations. In order to evaluate the
33 efficacy of irrigation, it is necessary to develop tools capable of evaluating root functioning and quantifying root water
34 uptake. The partial root zone drying (PRD) and RDI (Regulated Deficit Irrigation) methods are part of an ensemble of deficit
35 irrigation (DI) strategies that aim at improving water use efficiency. The PRD, for instance, consists of irrigating only one
36 part of the root system of the same plant using a certain percentage of the potential evapotranspiration (ET_p), usually inferior
37 to the total water needed. Application of DI triggers a physiological response in the plant via a hormone called Abscisic acid
38 (ABA), which is produced in the roots and transmitted to the leaves to regulate the stomata closure and thus reducing water
39 transpiration while keeping photosynthesis active and finally leading to increased water use efficiency (as reviewed in
40 Loveys et al., 2000; Davies et al., 2002). Notably, if there is adequate sap flow through the roots, the ABA signal is
41 transmitted through the xylem to the leaf, as demonstrated by Dodd et al. (2008). According to Davies and Hartung (2004), it
42 is proposed that plants subjected to partial root-zone drying (PRD) demonstrate improved performance compared to plants
43 under deficit irrigation (DI) when an equal amount of water is applied. This is attributed to the ability of PRD to stimulate
44 root growth and maintain consistent signalling of abscisic acid (ABA) to regulate shoot physiology. Davies and Hartung
45 (2004) stated that the effects of PRD on plant growth, yielding and functioning are quantitatively different from those of
46 RDI. One of the advantages of PRD when operated properly, is that plants sustained and even increased shoot and fruit
47 turgor even though a reduced amount of water is applied to roots (Mingo et al., 2003). On the other hand, one of the
48 disadvantages of RDI is that the entire root zone is allowed to dry out, the roots can become stressed and damaged and if not

5

2

6

rewetted can die and signalling may diminish. Conversely Fernández et al. (2006) stated that not always a PRD treatment has been found advantageous as compared to a companion regulated deficit irrigation (RDI) treatment and demonstrated it in a study on olive trees in which sap flow measurements, which reflected water use throughout the irrigation period, showed no evidence of stomatal conductance being more reduced in PRD than in RDI trees. Collins et al. (2009), in an experiment on the grapevine (*Vitis vinifera* L.) show that the response to PRD applied at 100% ETC and deficit irrigation applied at 65% ETC was the same, increasing stomatal sensitivity to vapour pressure deficit and decreasing sap flow. According to Cai et al. (2022), while stomatal conductance is a significant aboveground hydraulic factor influencing water use in crops, it should not discount the role of belowground hydraulics, as changes in soil-plant hydraulic conductance have been found to drive stomatal closure (Abdalla et al., 2021). This highlights the crucial importance of studying electrical activity in the soil. The plant's natural bioelectrical activity is necessary for its physiological processes. Plant scientists represent it by a water column where the ions move from bottom to top and vice versa due to gradients of water potentials. In their studies, Voytek et al. (2019) and Gibert et al. (2006) successfully linked the measurements of electrical potential in the ground and in the tree stem to the RWU and sap flow respectively. The use of active methods such as electrical resistivity tomography (ERT) allows for spatial and temporal analysis of the subsoil. Recent advances in electrical tomography imaging, in particular reduced at the plant scale, show their effectiveness to measure changes in soil water content associated with the RWU (e.g. Cassiani et al., 2015, 2016; Mary et al., 2018). Note that the correlation between root water uptake and soil water content changes exists when averaged over a larger spatial scale than the scale at which soil moisture redistribution can compensate for local root activity. The determination of these spatial scales depends on the soil hydraulic properties. This correlation between root water uptake and changes in soil water content can also be influenced by the time scales in addition to spatial scales. The ability to discriminate between them relies on factors such as the soil hydraulic properties, rates of local water extraction, and the temporal dynamics of water redistribution in the soil (Anonymous Reviewer, 2023). Applications of geoelectrical methods to evaluate water use efficiency are increasing. Recently in an experimental Citrus orchard, Consoli et al., (2017), Vanella et al., 2018 and Mary et al., (2019a) showed that the observed drying pattern resulting from an elevated evapotranspiration rate (ER) in the non-irrigated section of the root zone matches the root distribution in that area, while the

10

73 observed wetting pattern arising from a decreased ER in the irrigated section of the root zone can be attributed to the
74 irrigation itself.

75 However, processes occurring in the rhizosphere can affect the soil ER in various ways. Roots induce changes in the soil
76 structure in terms of porosity and hydraulic conductivity which ultimately modify the water pathways and fluxes and thus the
77 ER itself. Soil structure changes may have a relatively smaller effect on ER than root water uptake RWU, although this may
78 differ for species with extensive root systems like woody species; this is further true during rainfall or irrigation considering
79 water redistribution and channelling influenced by varying root anatomies and causing dynamic variations in ER. Stemflow
80 channelling by roots is an example of how water from rain or irrigation can be driven to soil recharge by the root structure.
81 Conversely, root uplift in agroforestry shows how water can move from the deeper layers to the top via the roots. Roots also
82 affect the soil ER through the geochemical changes associated with root exudates and root symbiosis. At the interface
83 between soil and roots, the chemical gradients and concentrations can drastically differ from those observed in the soil
84 regions not affected by the roots. Although this can have a significant impact and be a valuable source of information, only a
85 few studies have extended the ERT and the induced polarisation (IP) to observe these changes (Weigand, 2017; Weigand
86 and Kemna, 2019; Tsukanov and Schwartz, 2020, 2021). As of today, the electrical behaviour of individual roots remains
87 poorly understood, particularly with regard to their changes in type (from hair roots to fully lignified roots), space, time, and
88 whether the root is active or not (Ehosioko et al., 2020).

89 The geophysical approach extends the scope of traditional methods to evaluate soil water content (SWC) using time-domain
90 reflectometry (TDR) sensors and the calculation of RWU (Jackisch et al., 2020). In the field, the spatial resolution is
91 controlled (in ERT or IP) by the arrangement of the electrodes and acquisition parameters (Uhlemann et al., 2018), while the
92 temporal resolution is controlled by the time it takes to complete a full sequence measurement.

93 Rhizotrons are one of the earliest and most effective tools for studying root growth and functioning, both in the field and in
94 the laboratory (Taylor et al., 1990). They are transparent boxes that allow the direct observation of the roots during plant
95 growth and changes in soil conditions. Rhizotrons also provide valuable support in multidisciplinary studies, allowing other
96 methods to be more easily and precisely deployed, so that their results more reliably interpreted. For example, a load scale is
97 often mounted in combination with the rhizotron in order to weigh the system, which allows inferring the quantity of water

11
12

98 lost by the plant over time. This set-up is inspired by the lysimeter and is widely adopted to measure the water balance of the
99 soil-plant interactions. For example, in a rhizotron, Doussan and Garrigues (2019) use the light transmission 2D technique
100 to infer root water uptake with respect to their genotypes.

101 The very few studies conducting geophysical tomography imaging in the laboratory using a rhizotron proved a certain
102 efficiency in studying the interaction between soil physics and plant physiology for predicting plant response to
103 environmental stresses (Weigand, 2017, 2019; Peruzzo et al., 2020). It allows for high-resolution tomography by reducing
104 the size, diameter, and spacing of the electrodes. The entire soil profile is easily accessible by placing electrodes on the side
105 of the rhizotron, easing the depth resolution limitation inherent to surface-based geophysical methods usually used for field
106 acquisition.

107 Although there is a good momentum for the use of geophysical methods applied to agronomy (Garré et al., 2021), a number
108 of gaps still need to be addressed. All the indirect root effects on the soil ER affect the evaluation of the soil water content,
109 making the interpretation of ERT to quantify RWU sometimes difficult (Ehosioko et al., 2020).

110 **1.1. Current pathways in roots under water stress constraints**

111 Current pathways in roots remain certainly the main unknown since there is a gap in techniques to measure
112 it non-destructively (Ehosioko et al., 2020; Liu et al., 2021). The current pathways in roots are possibly
113 linked to RWU. Lovisolo et al. (2016) describe in detail the flow of water from root water uptake and the
114 processes occurring at the cell scale. In any case, root water uptake is not distributed equally over the
115 whole root system, in part, due to heterogeneous soil conditions. For the same reason as soil saturation can
116 change over time, RWU is also varying in the time. The concept of active roots has been previously
117 employed by several authors (Frensch and Steudle, 1989; Doussan et al., 1998; Garrigues et al., 2006;
118 Srayeddin and Doussan, 2009) to characterise the spatial variability of root water uptake. In this context,
119 plants adapt by reducing radial conductivity in dry regions, enabling them to redirect their uptake towards
120 wetter areas with higher soil conductivity. This mechanism allows plants to maintain a consistent rate of
121 water uptake while sustaining higher plant water potentials. For active roots, root water uptake consists in
122 a moving water from the root tip (which is usually much more electrically conductive due to high water

123 conductivity at its proximity) in the radial direction via cellular (symplastic way) and between cells
124 (apoplastic way) until it reaches the xylem which transport it in the axial direction towards the upper part.
125 Water flow can encounter resistances due to suberization (conversion of the cell walls into cork tissue by
126 development of suberin), which is naturally driven as a consequence of root growth (secondary roots are
127 more suberised than primary roots) but it can also be the consequence of plant stress (Malavasi et al., 2016;
128 Song et al., 2019). The process can cause reductions in water conductivity through the root system by
129 limiting the permeability of the root tissue, thus leading to changes in the plant's ability to take up water.
130 Aroca et al. (2012) describes in a generic manner the plant responses to drought stress. For the specific
131 PRD case, there is a complex tradeoff induced by root suberization between reducing radial flow (as a
132 consequence of ABA signalling sent by the roots) to conserve water in the soil but keeping the axial flow
133 active. This can be done for instance by adjusting the xylem vessels size and quantities. Although
134 suberisation is usually a long-term process, studies show that PRD can promote and accelerate the process
135 of suberization in response to water limitation. Finally during PRD conditions we can also observe transfer
136 of water from the wet to the dry side through the roots (overnight) in a process called redistribution (Yan et
137 al., 2020), which induces spatio-temporal variations in RWU that ultimately also influences electrical
138 current pathways in roots.

139 A direct approach to analysing the active part of the root system consists of an injection of current stimuli
140 into the plant stem. There is a variety of stem based methods used in the literature with applications
141 ranging from biomass estimation, root morphology to root physiology (root activity). At a single
142 frequency, we distinguish between ECM methods which rely on capacitance measurements and are
143 commonly used to study root systems at the plant scale and EIM, which measures both capacitance and
144 resistance. Capacitance represents the polarization processes and measures the charges stored during the
145 current flow. Both use the fact that the root can polarise at the soil-root interface and inside the root to
146 infer direct root-related information such as dry and wet mass, surface area,...). A second group of methods
147 Electrode Impedance Spectroscopy (EIS) uses a range of frequencies to capture the polarisation processes

148 sensitive to the root physiology and anatomy. For a detailed description of the methods, the reader is
149 invited to refer to (Ehosioko et al., 2020). The stem based approach has been developed for years by plant
150 physiologists, starting from the theory developed by Dalton (1995) who conceptualized the current
151 pathways through the root xylem by an equivalent parallel resistance-capacitance circuit. The theory holds
152 under the assumption that the current flows throughout the most conductive path and is held (thus inducing
153 polarization) by the root cell membranes before being released into the soil. Fine root connections and
154 mycorrhiza facilitate the efficient transfer of injected current into the soil at contact points between roots
155 and the soil, resulting in a distribution of current sources within the ground. Contrasting experimental
156 results have challenged the relationship between root electrical capacitance and root traits in different
157 crops, with studies highlighting the potential contribution of the stem, rather than the roots, to the overall
158 measured root electrical capacitance and the occurrence of current leakage at the proximal part (Urban et
159 al., 2011; Dietrich et al., 2018; Peruzzo et al., 2020).

160 Without being able yet to give hints about the electrical current pathway, recent advancements in the
161 development of explicit RWU models, based on plant hydraulics, provide insights into how robust
162 capacitance models hold and under which conditions. We learnt, for instance, that at the root level, RWU
163 models account for the anisotropy by separating the root hydraulic conductance into two terms i.e. axial
164 and radial (Javaux et al., 2008; Couvreur et al., 2012). Figure 1 draws inspiration from the electrical circuit
165 analogy of RWU (Root Water Uptake) proposed in previous works (Doussan et al., 1999, Manoli et al.,
166 2014 and Couvreur et al., 2012 and Cai et al., 2022). In dry soil conditions, the primary part of the
167 potential drop happens within the soil-to-root connection, while in wet soil conditions, the main portion of
168 the potential drop is in the plant section. in dry soil, the gradient $\Delta\psi_{\text{soil}} = (\psi_{\text{soil}} - \psi_{\text{soil-root}})$ is higher than in wet
169 soil. As the soil conductance g_s is linked by the relationship between the transpiration rate over the $\Delta\psi_{\text{soil}}$,
170 for the same evaporation rate, g_s is decreasing when the soil dries out. The root axial water flow rates Q_x
171 (L^3T^{-1}) and root radial water flow rates Q_r (L^3T^{-1}) can be solved analytically by solving the system of
172 equations of Ohm's and Kirchhoff's laws (Couvreur et al., 2012).

22

173

174

175

176

177

178

179

180

181

182

183

184

185

186

187

188

189

190

191

192

193

194

195

196

197

The same applies to the stem-based methods as root hydraulic conductance and electrical conductivity are likely to vary conjointly. Up to now the relationship between root water content and root hydraulic conductivity with ER has not been firmly established. Many other parameters such as root function, age, water retention capacity and transpiration rate in particular can affect the water flow as well as the current pathway of stem-based methods (Ehosioko et al., 2020).

Peruzzo et al. (2020) hypothesize that drought stress can also reduce electrical current leakage wherein the current exiting the plant root at the proximal part is decreased, particularly for woody species. Furthermore, as expected, the frequency of the injected current plays an important role in the capacitance measured. At high frequencies, both the longitudinal conductivity and radial conductivity increase (Mancuso 2012; Ehosioko et al. 2020), which can also cause current leakage problems (Gu et al., 2021). The measure of plant responses over multiple frequencies, a method called Electrical Impedance Spectroscopy (EIS) is more time-consuming but more informative since different polarisation processes can manifest themselves in the signal (Ehosioko et al., 2020). The contrast of electrical resistivities between soil and roots plays a fundamental role as reported e.g. by Cseresnyés et al. (2020). Gu et al. (2021) stated that the potential to directly quantify root traits under dry conditions is higher than under wet conditions and interpreted this as a result of the fact that the root electrical longitudinal conductivity is higher than that of the soil under dry conditions. The instrumentation and acquisition schemes used for impedance are also questionable and the optimal experimental setup of measurement remains to be determined (Postic and Doussan, 2016). The number and the position of the stem and the return electrodes are a cause of uncertainties (electrode contact resistance, etc.). Peruzzo et al. (2021), in a three channels experiment, were able to provide direct access to the response of stem and soil, which ultimately allowed the decoupling of the root response. Evidence showed the presence of current leakage in herbaceous root systems, a significant contribution from plant stem, and a minor impact from the soil.

23

24

198 Gu et al. (2021) stated that in addition to the traditional regression model used for predicting root traits
199 using the impedance method, a forward model would help to illustrate the importance of these different
200 factors. In order to cope with the main drawbacks of the impedance methods, we propose the so-called
201 Electrical Current Imaging (ECI) method, a physically based approach based on recovering the current
202 density distribution instead of simply calculating the total resistance/capacitance. This method is also
203 referred to as *mise-à-la-masse* (MALM) in the applied geophysics literature. The current imaging methods
204 hold some promise to offer a first set of evidence about the current pathways: This is a popular technique
205 adopted e.g. by the neurosciences community, where the current density in the human brain correlates with
206 diverse patterns of neural activity (Kamarajan et al., 2015). Peruzzo et al. (2020) applied it for plant roots
207 imaging with relative success, as the authors stated that all the current leaks at the plant's proximal part i.e.
208 at the shallowest contact of the plant stem with the soil. For the ECI approach, the Poisson's equation
209 serves as a physical model for the electrical current flow. As current flow is modulated by the conductivity
210 of the soil, the ECI approach is always combined with ERT in order to recover of the soil resistivity
211 distribution.

212 **1.2. Study aims and assumptions**

213
214 The aim of this study is twofold:

215 (i) we aim at showing the correlation between the current path through the root system and the active root
216 zones. This assumption is based on the notion that soil and root hydraulic conductances are positively
217 associated with electrical conductances.

218 (ii) we want to investigate how the soil water content affects the current path.

219 For this, we rely on the following assumptions:

220 - changes in soil water content measured by ERT are a relevant spatial proxy of root activity and can be
221 used as an indicator of the actual plant transpiration by correlating them with variations of the total
222 rhizotron measured weight.

223 - During the implementation of root-zone limited water availability, when a portion of the root system in
224 the dry zone becomes deactivated, injected current in the stem tends to preferentially propagate towards
225 the side where the root system is irrigated.

226

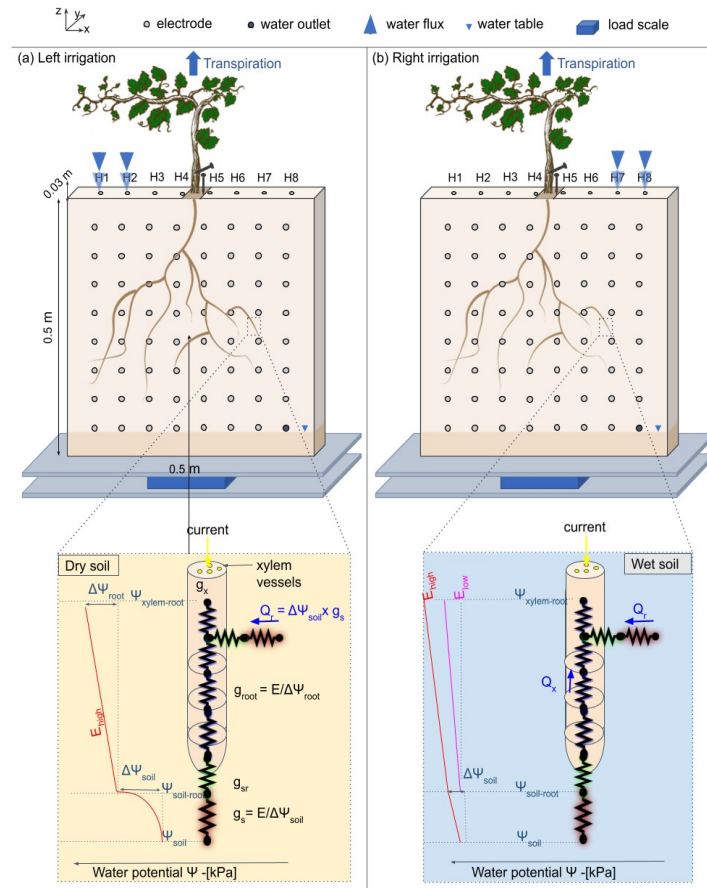
227 **2. Material and methods**

228

229 **2.1. Experimental setup**

230 **2.1.1. Rhizotron**

231 The experiment was conducted using a rhizotron 50 cm wide, 50 cm high, and 3 cm thick, with a
232 transparent screening face. The front of the rhizotron was equipped with 64 stainless steel
233 electrodes with 4 mm diameter which did not extend into the rhizotron's inner volume (Fig. 1).
234 An additional line on the top surface of the rhizotron was composed of 8 electrodes inserted to 1
235 cm depth. A growth lamp was installed above the rhizotron and turned on during daylight hours
236 (from 7 am to 7 pm). The rhizotron was closed on all sides and watertight, with only 8 small holes
237 used for the irrigation at the surface and the central hole where the plant is placed. We considered
238 the surface of these holes to be sufficiently small to neglect the possible effect of evaporation
239 through them. An outlet point was placed on the bottom right side ($z=5\text{cm}$) and the rhizotron was
240 always saturated below this point. In the course of the experiment (after the growing period) no
241 water discharge was observed through the outlet point.



243 **Figure 1: Conceptual figure showing the position of the plant in the rhizotron. The water input was done alternatively from left (a)**
 244 **to right (b) via small holes on the top of the rhizotron (H1 to H8). The roots are free to grow on both sides of the rhizotron. The**
 245 **circles on the screening face show the locations of the electrodes. Two additional electrodes (needles) are used for the ECI, one for**
 246 **the stem injection and the other for the control soil injection next to the stem. The rhizotron is weighted by a central point load**
 247 **scale (PC60-30KG-C3, Flintec) mounted between two support plates in plexiglass. The line below describes the state of the art of**
 248 **hydraulic conductivity at a single root and the distinction between dry (c) and wet (d) soil. The figure draws inspiration from the**
 249 **electrical circuit analogy of RWU (Root Water Uptake) proposed in previous works (Doussan et al., 1999, Manoli et al., 2014 and**
 250 **Couvreur et al., 2012 and Cai et al., (2022)). In a recent article, Cai et al. (2022) schematized the gradient of potential ψ_{soil} , $\psi_{\text{soil-root}}$**
 251 **and ψ_{root} , along with the corresponding hydraulic conductances of the soil, the soil-root interface, and the root (represented as g_s ,**
 252 **g_{sr} , and g_r , respectively), in response to high or low transpiration demand (E). Note that the soil-root interface and the xylem cell**
 253 **interfaces are seats of current polarization due to the formation of the Electrical Double Layer (EDL) well described in Tsukanov**
 254 **and Schwartz (2021).**
 255

256

2.1.2. Plant treatment

257

258

259

260

261

262

263

264

2.1.3. Soil type

265

266

267

268

269

270

271

272

273

2.1.4. Irrigation schedule

274

275

276

277

278

At the initial stage of the experiment, we used a *Vitis Vinifera* cutting with a pre-developed root system (rooted cutting var. Merlot) was used. The cutting was grown in hydroponic solution (modified Hoagland medium) for 4 months before being transferred into the rhizotron. This was followed by a growing period of 5 weeks with irrigation applied over the whole width of the rhizotron every 3 days. The vine was then irrigated with a nutrient solution (see Table 1) following a PRD protocol.

The experiment was conducted in a sand-peat mixture (50-50 m/m%). The applied sand was high-purity quartz sand ($\text{SiO}_2 = 99\%$) of grain size comprised between 0.1-0.6 mm and the peat was a normal commercial acidic sphagnum peat. During the course of the experiment, the soil was stable through time with very low compaction (1 cm) observed at the end of the experiment (already observed by Doussan & Garrigues, (2019) for soil with a lower density than 1.5-1.6 g/cm^3). The sand-peat mixture was chosen as a compromise between water retention and drainage. We estimated the porosity at the beginning of the experiment as equal to 55% using the ratio of water weight after saturation to the total volume of the rhizotron.

We controlled the water supply for each irrigation event based on the data obtained from the scale, ensuring that the plant received 75% of the measured transpiration accumulated since the last irrigation cycle. For each cycle, the wetting side changed (from left to right). Note that in this experiment, we did not consider a physical barrier to separate the two sides of the rhizotrons to a split-roots configuration as is the case for other PRD experiments conducted in the laboratory

37

279 (Martin-Vertedor and Dodd, 2011; Sartoni et al., 2015). In general, the use of physical barriers in
 280 Partial Root Zone Drying (PRD) experiments is not always a standard aspect of the setup.

281 Table 1 describes all cycles conducted from May 13th to July 12th 2022:

- 282 - The goal of Cycle number 0 was to ensure plant adaptation and growth after
 283 transplantation.
- 284 - Cycle numbers 1 to 3 aimed at starting the PRD irrigation with half of the rhizotron
 285 volume irrigated; i.e. we irrigated the side through a total of four holes out of eight (see
 286 Fig. 1).
- 287 - From cycle number 4 to 10, we restricted the water input only to the two left/right most
 288 holes.
- 289 - Between cycles 4 and 5, we added intermediate irrigation on the full length of the
 290 rhizotron.

291 For the irrigation, we used a nutrient solution (modified Hoagland) (Hoagland and Arnon, 1950)
 292 having an electrical conductivity equal to $2470 \pm 5 \mu\text{S}/\text{cm}$ (at $\sim 25^\circ\text{C}$), except for cycle 3 where tap
 293 water was used ($560 \mu\text{S}/\text{cm}$).

294

Irrigation time (YYYY-mm-dd HH:MM)	Hole (H) location (c.f. Fig. 1)	Quantity (mL)*	Cycle nb
2022-05-13 16:25	All		0
2022-05-19 17:00	H1;H2;H3;H4	200	1
2022-05-25 14:30	H5;H6;H7;H8	260	2
2022-06-01 15:50	H1;H2;H3;H4	290	3
<i>2022-06-08 11:50</i>	<i>H7;H8</i>	<i>305</i>	<i>4</i>
<i>2022-06-10</i>	All	60	- (<i>4bis</i>)
2022-06-15 17:25	H1;H2	350	5
<i>2022-06-22 16:45</i>	<i>H7;H8</i>	<i>375</i>	<i>6</i>
2022-06-29 13:45	H1;H2	386	7
<i>2022-07-05 18:10</i>	<i>H7;H8</i>	<i>431</i>	<i>8</i>
2022-07-11 13:15	H1;H2	431	9

295

296 **Table 1: Irrigation log, indicating the irrigation initial time, the location where the water was input**
 297 **and the corresponding cycle number considered in the results. The font correspond to the side used**
 298 **for the irrigation, bold is on the left side while italic is on the right side. * Quantity in total**
 299 **distributed over all the holes.**

38

39

300 2.2. Electrical Resistivity Tomography

301 Electrical Resistivity Tomography consists in reconstructing the subsoil ER using an array of electrodes
302 (Binley and Slater, 2020). In this study, a total of 72 stainless steel electrodes were used, 64 electrodes
303 formed a grid, 5 cm spaced, covering the screening face of the rhizotron, and an additional line of 8
304 electrodes was posed at the top surface. Electrodes are needles 4 mm in diameter and 80 mm in length, but
305 only their tip is in contact with the soil. ERT involves the measurement of transfer resistances following a
306 sequence describing a combination of varying injections (AB) and potential (MN) pairs of the electrodes.
307 We used a custom sequence composed of 4968 quadrupoles including the reciprocals (e.g. Parsekian et al.,
308 2017), and the measurement were conducted using a Syscal Pro (Iris Instrument) resistivity meter., The
309 sequence was optimized over the ten physical channels of the instrument in order to reduce the acquisition
310 time to approximately 30 min. The data acquisition parameters were constant along the monitoring, with a
311 minimum required V_p of 50 mV, a maximum injection voltage V_{AB} of 50 V, and a number of 3-6 stacks
312 with the on-time fixed to 250 ms each.

313 2.3. Electrical Current Imaging

314 The electrical current imaging (or Mise-à-la-masse) method was logistically similar to ERT. The sequence
315 nevertheless varies, as the pairs of injection electrodes were kept constant with the positive pole (+I)
316 electrode located on the stem, and the return (-I) electrode located in the bottom right of the rhizotron. The
317 potential electrodes pairs (MN) vary according to a custom sequence. For the stem current stimulation, we
318 inserted a small stainless steel needle (2 cm, 1 mm diameter) into the plant stem at 5 cm from the grafted
319 point. The needle was inserted all the way to the centre of the stem (Fig. 1). Before each measurement, we
320 added a few drops of water to the stem needle in order to reduce the stem contact resistance (to values
321 between 41 and 66 k Ω). The current was guided to the root system via the stem and then released into the
322 soil.

323 As the effect of the stem contact resistance affects the measured voltage, a control soil injection was
324 systematically made. In that case, the current was injected into the soil close to the plant (Fig. 1). A

325 qualitative comparison between the control soil injection and the stem injection plant could be made to
326 discriminate the effect of roots. Furthermore, soil control injection served as a visual calibration for the
327 inversion of the current source knowing that the injection is punctual and occurs at a known position.

328

329 **2.4. Weight monitoring for the estimation of transpiration**

330 In order to track the weight changes due to the transpiration of the plant, the rhizotron was equipped with a
331 single point load cell (PC60-30KG-C3, Flintec), mounted between two plates in plexiglass supporting the
332 rhizotron (Fig. 1). The data were logged with a sampling rate of 5 min using the weight indicator DAD-
333 141.1. The total weight of the rhizotron is about 20 kg and the expected resolution according to the sensor
334 datasheet is 0.1 g. The variation due to temperature was monitored, on average in May at 22°C, and in July
335 at 25°C. To avoid sharp signal perturbation, during the irrigation and the acquisition of geophysical data
336 the logger was paused.

337 **2.5. Leaf gas exchange observations**

338 In order to monitor the physiological response of the plant during the course of the experiment, stomatal
339 conductance to water (g_{sw} [$\text{mmol H}_2\text{O m}^{-2} \text{s}^{-1}$]) measurements were performed on vine leaves with an open
340 flow-through differential porometer (LI-600, Li-Cor Inc., Lincoln, Nebraska, USA). The stomatal
341 conductance is a measure of the density, size, and degree of opening of the stomata, therefore it can be
342 used as an indicator of plant water status (Gimenez et al., 2005). The measurements were carried out on 26
343 leaves in the morning hours (at 10 a.m.), once (on 8th June 2022) just before irrigation (severe water
344 stress), and once (on June 16, 2022) one day after irrigation (mild to low water stress). For the tracking of
345 the plant development, the length (L) and the width (W) of every leaf were measured every 2 weeks from
346 the beginning of the growing period until the end of the experiment. From this data the total leaf area (LA)
347 was estimated according to three models: $LA1 = 0.587 (L \times W)$ (Tsialtas et al., 2008); $LA2 = -3.01 + 0.85$
348 $(L \times W)$ (Elsner and Jubb, 1988); $LA3 = -1.41 + 0.527W^2 + 0.254L^2$ (Elsner and Jubb, 1988).

349 2.6. Data processing

350 2.6.1. Analysis of ERT data

351 The ERT acquisition sequence was initially tested on the rhizotron filled with water of known
352 conductivity and it offered good coverage on most of the rhizotron surface with a slight decrease
353 on the sides. The soil electrode contact resistances varied over the course of the experiment
354 between 5 and 20 k Ω . Data were filtered on the basis of the percentage of variations between
355 direct and reciprocal measurements. We chose to eliminate the data with reciprocal relative errors
356 larger than 5%, for all the time steps. The number of rejected data varies from 9% to 39 % of the
357 total (see Table A1) with a median of 11%. Transfer resistances were inverted using the open-
358 source code ResIPy (Blanchy et al., 2020) based on the Fortran R3t code (Binley, 2015). The
359 inversion mesh is an unstructured grid composed of tetrahedra, created using Gmsh (Geuzaine
360 and Remacle, 2009). Two distinct strategies can be used: (1) individual inversion which consists
361 of building a model of resistivity at a given time, and (2) time-lapse inversion (difference
362 inversion) where the difference in resistivity is inverted between a given survey and a background
363 survey (in this case, the background survey is the previous one). In this study, we used the first
364 approach, which allowed filtering of systematic noise and highlights variations (as a percentage of
365 differences) between two times.

366 2.6.2. Analysis of current density

367 The mathematical formulation for the inversion of the current source density (CSD) has been
368 developed in previous studies. It consists in searching for a linear combination of Ohm's law, for
369 a series of current punctual sources (also called virtual sources) minimizing the misfit between
370 simulated and observed data. The algorithm was initially tested on the rhizotron filled with water
371 of known electrical conductivity and a single isolated cable (see the procedure from Peruzzo et
372 al., 2020). It is important to note that the CSD inversion relies on the knowledge of the medium
373 conductivity (as in the Poisson's equation, the current is modulated by the electrical conductivity).

374 Thus, we used the inverted ER values as the resistivity distribution for the forward modelling in
 375 the current density inversion. As for ERT, choices must be made on how data and models are
 376 weighted and regularised during the inversion. In this study, we run unconstrained (no prior
 377 information) inversions for all the time steps with a regularisation (smoothing using the first
 378 derivative). The numerical routine includes a “pareto” functionality wherein regularization and
 379 model-to-measurement fit are traded off to estimate the optimum regularization weight w_r . The
 380 code used for this inversion is available at <https://github.com/Peruz/icsd>.

381 **2.6.3. Calibration of petrophysical relationships**

382 In order to estimate the soil water content in the rhizotron during the experiment, we needed to
 383 adopt a suitable constitutive model, starting from the available ER measurements.

384 Archie's (1942) law (eq. 1) is a widely used empirical relationship that relates the ER (ρ) of a bulk
 385 material to its porosity (Φ), the contained fluid (water) electrical resistivity (ρ_f) and the fluid
 386 saturation (S). Archie's parameters a , m , and n are empirically derived, generally named as
 387 follows: a is the tortuosity factor, m is the cementation exponent and n is the saturation
 388 exponent.

$$\rho = a\rho_f\phi^{-m}S^{-n} \quad (1)$$

389 We calibrated these parameters experimentally, as usually done, by collecting water saturation-
 390 ER values over different soil samples. The sample holder (a cylinder of 150 mm inner height and
 391 41 mm inner diameter) allows for a four-point measurement of the ER converted to apparent ER
 392 using the appropriate geometrical factor. The adopted water electrical conductivity is known and
 393 fixed (594 $\mu\text{S}/\text{cm}$ at $\sim 25^\circ\text{C}$). The rhizotron soil mixture porosity was assumed to be equal to
 394 0.55, . The sample was initially saturated to field capacity and progressively desaturated. The
 395 field capacity was estimated by gravimetric method approximately at 40% of volumetric water
 396 content (m^3/m^3). In total, 6 measurements were collected at respectively 40, 33.6, 29.7, 28.2, 25.2,

397 22.4% of volumetric water content (m^3/m^3). The obtained data are fitted with a least square
398 optimization (using the Scipy library by Virtanen et al., 2020). Here we assume a equal to 1
399 (consistent with the theoretical value), while the exponents m and n are bounded during the
400 optimization process to respectively [1.3-2.5] and [1 - 3]. With a coefficient of determination R^2
401 of 0.97 (figure not shown), we obtained values of 1.9 and 1.2 respectively for m and n .

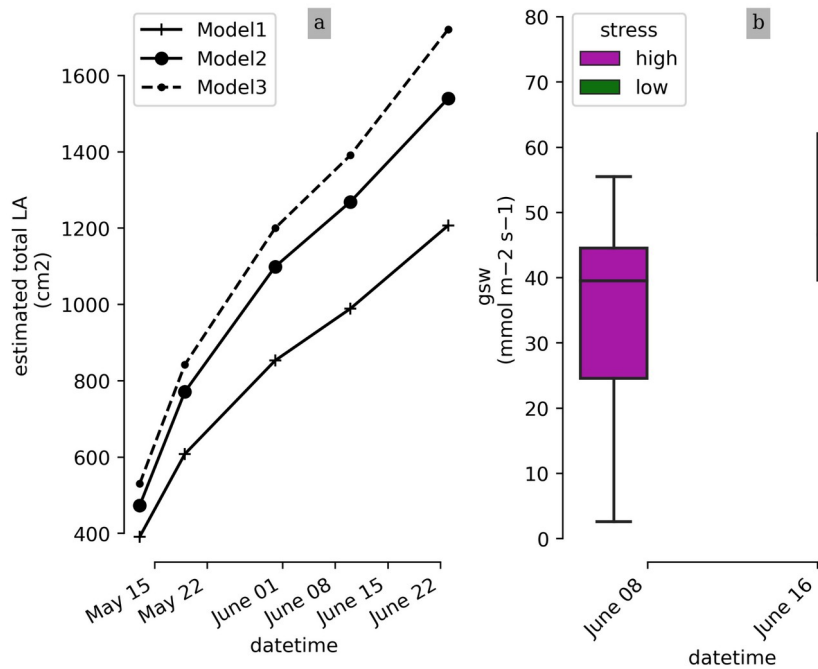
402 3. Results

403 3.1. Physiological response

404 Photographs of the plant at the beginning and at the end of the experiment show the increment of leaf area
405 extension of the aerial part. The weekly measurements show a linear trend with time of the estimated total
406 LA (cm^2) whichever the model used (Fig. 2). At the end of the experiment water stress symptoms
407 were visible on some leaves.

408 As for the root system, the depth variations could not be precisely assessed during the course of the
409 experiment. We observed that: (i) roots reached the bottom part of the rhizotron; (ii) spread all over the
410 rhizotron with a network of primary, secondary, and root hairs without any given architecture (some roots
411 grew vertically, others in diagonals); (iii) the roots kept a white appearance with apparently no lignification
412 even for the largest roots ($\geq 3\text{mm}$).

413



414

415

416

Figure 2: (a) Time evolution of the estimated total leaf surface area (LA) for three different model estimators. (b) leaf stomatal conductance (High and low stress distributions are significantly different with a T-test p -value = $4.3 \cdot 10^{-3}$)

417

418

419

420

421

422

423

424

425

3.2. Transpiration rate

426

427

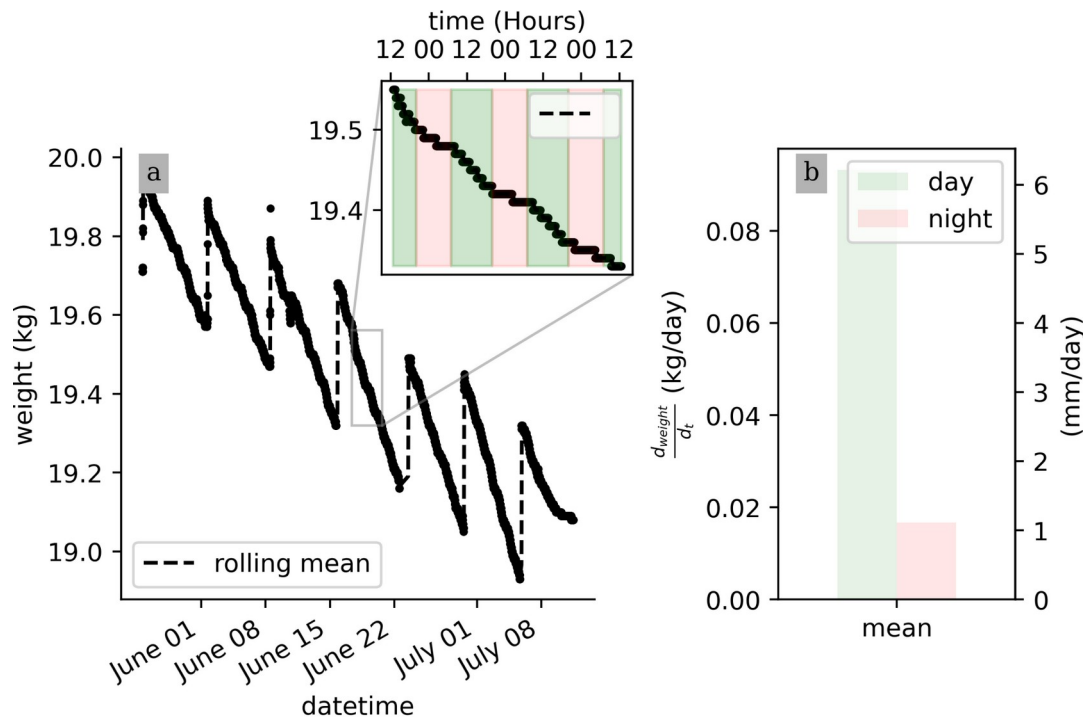
428

The measurements shown come from the 26 leaves (c.f section 2.5) and indicate that the plant is under high water stress at the end of the irrigation cycle (one week after the last partial irrigation, on June 8, 2022), and under lower water stress one day after irrigation (on June 16, 2022). The mean, min, and max values of the stomatal conductance (g_{sw}) values are 37.8; 23.3; 55.5 mmol m⁻² s⁻¹ before irrigation, respectively, and 50.6; 18.9; 78.1 mmol m⁻² s⁻¹ after irrigation, respectively. The result of the T-test shows that their mean values are significantly different (p -value = $4.3 \cdot 10^{-3}$).

56

57

429 content is decreasing, the transpiration rate (slope of the weight variations) remains constant for each
 430 cycle. At the very end of the experiment from July 9, an inflexion point is observed and the weight stops
 431 decreasing. Zooming on a shorter time window, the variation of the raw data weight clearly shows
 432 day/night patterns triggered by the hours when the light is switched on/off. On average, the water lost
 433 during the day is nearly 20 times more than during the night (0.09 kg/day against 0.005 kg/night). Note
 434 that there is no distinction between the hours of the day (due to artificial lighting).



438
 439 **Figure 3: Raw scale data collected over the course of the experiment (a) and a zoom on the week of June 20 to 25, where day and**
 440 **night periods are respectively highlighted by the green and red shaded areas. (b) Calculated daily mean transpiration (d_{weight}/d_t)**
 441 **during the day (green) and night (pink) periods.**

61

442

443

3.3. Time-lapse ERT

444

445

446

447

448

449

450

451

452

453

454

455

456

457

458

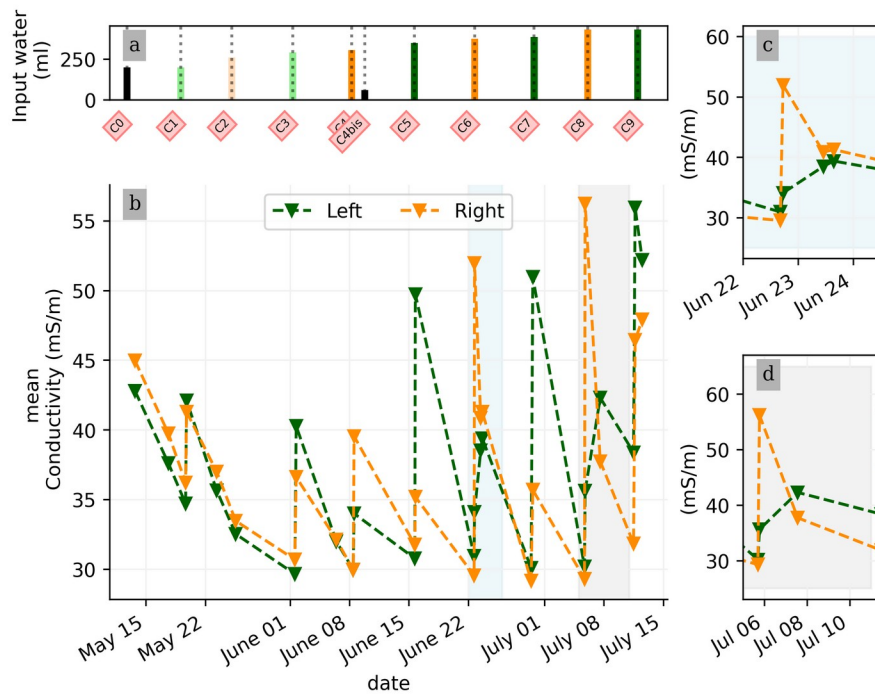
459

460

In general, the ERT data quality is very good with a small percentage of total measurements exceeding a reciprocal noise level of 5% (see Fig. A1 to A11) and with each inversion resolved within 2/3 iterations. Figure 4 shows the trend for the PRD cycles (from cycles 0 to 9) for the mean average electrical conductivity (in mS/m) for both the wet and dry sides of the rhizotron, taken as an average of each half of the ERT inversion mesh elements. When PRD is applied over only two holes (from cycle 4) the irrigated side shows a clear increase in electrical conductivity. To a much lower degree, the dry side is also affected by the water input, likely due to water redistribution during drainage. When available, the temporal dynamics between two irrigations show that the conductivity is decreasing rapidly on the irrigated side during the 2 first consecutive days and more slowly afterwards (cycles C5/6 and C7/8 respectively; Fig. 4c and Fig. 4d). As some water infiltrates also on the dry side, we also observe an increase in conductivity in it. At the end of each cycle (the cycle length is about 7 days), the rhizotron returns to the equilibrium condition, with a more homogeneous and stable average conductivity equal to 30 mS/m (mean of the dry and wet sides). This is generally true for all times, except at the end of the experiment, cycles 7 and 8, when the two sides are in different conditions.

62

63



462

463 **Figure 4: (a) Evolution of the quantity (in ml) of water input, spatially distributed with alternating between left (green) and right**
 464 **(orange) before and during the PRD irrigation. (b) Evolution of the mean conductivity (mS/m) average on each side, markers show**
 465 **the acquisition time. (c) and (d) are inset zooms showing changes before and just after the irrigation event.**

466

467

468

469

470

471

472

473

474

475

We selected a time window between 29 June and 5 July showing the spatial variations of the ER before and after an irrigation event (Fig. 5). The application of background constraint inversion, as illustrated in Figure 5bc, leads to an interpretation suggesting that the blue regions correspond to areas where the soil is wet, whereas the red regions correspond to areas where the soil is drying. Before the irrigation, the top and left-most and right-most boundaries of the rhizotron exhibit higher ER (50 Ohm.m) than the central part (25 Ohm.m). One hour afterwards (+ 1H) the ER of the left irrigated side had dropped by 20% (estimated from the averaged values spanning from the middle of the rhizotron to the left boundary).

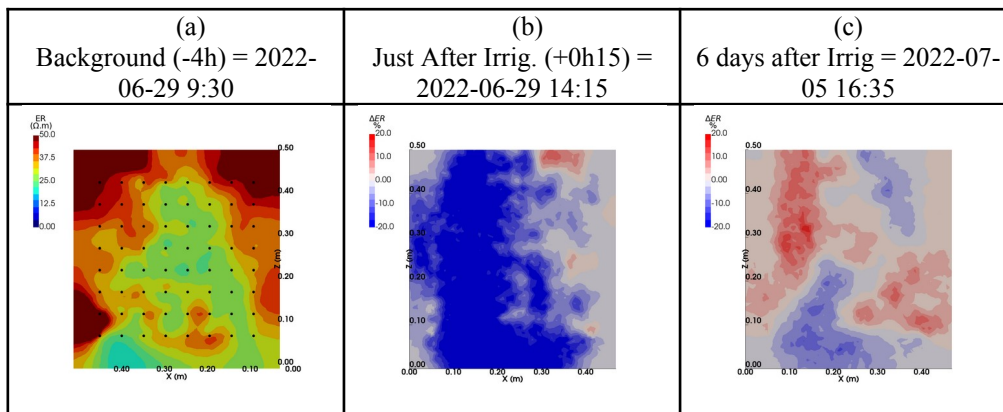
All time-lapse inversions before/after irrigation are shown in Appendix A, including before the PRD.

They all show that a decrease in ER is associated with irrigation patterns while an increase in ER has a

67

476 more complex spatio-temporal dynamics, not systematically associated with irrigation patterns. Positive
 477 alterations in resistivity observed immediately after the irrigation event may potentially be artifacts
 478 stemming from strong gradient in resistivity induced by the irrigation. Changes in ER after six days (day
 479 +6) show that RWU effects are not limited to the irrigated part since the increase of resistivity was also
 480 observed on the dry part. We noticed from a visual inspection of the rhizotron that a water table forms at
 481 0.4 m where the soil is saturated. This saturated zone level is not affected by the irrigation as no increase
 482 after irrigation, and no decrease by the end of the irrigation cycles are visible. We assume that most of the
 483 water fluxes were connected to the unsaturated part.

484



485

486 **Figure 5: Spatial distribution of the resistivity (in Ωm) and changes (in %) in ER obtained by a time-lapse inversion between cycle**
 487 **6 and 7 following partial left irrigation of the rhizotron. Time steps correspond to measurements before (a), 15 minutes (b) and 6**
 488 **days (c) after irrigation started.**

489

490 3.4. Time-lapse ECI

491

492 Figure 6 shows the trend of the horizontal location (x coordinate) of the centre of mass of current density
 493 during the PRD cycles (from 0 to 9), after the alternative wetting events on the left and right sides of the
 494 rhizotron. Considering the modulation of current by soil electrical resistivity (ER), any bias in ER could
 495 introduce errors in forward current source imaging and, consequently, affect the positioning of the current

68

69

70

496

497

498

499

500

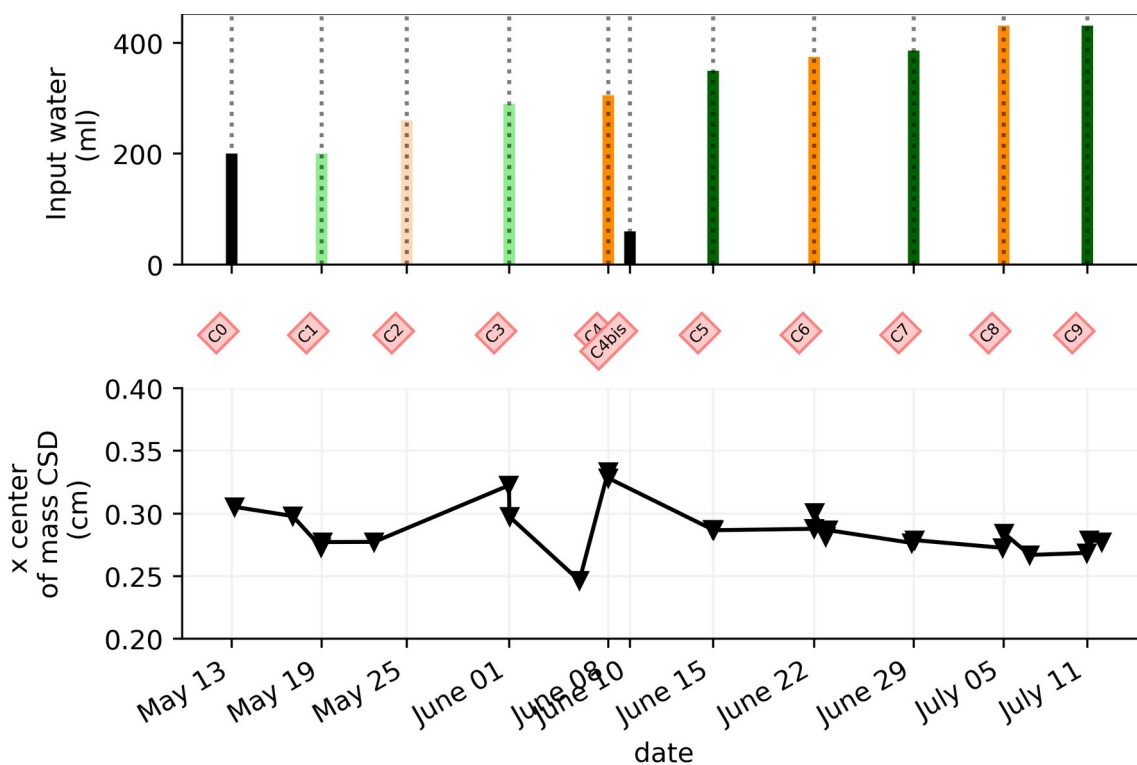
501

502

503

504

505



507

508

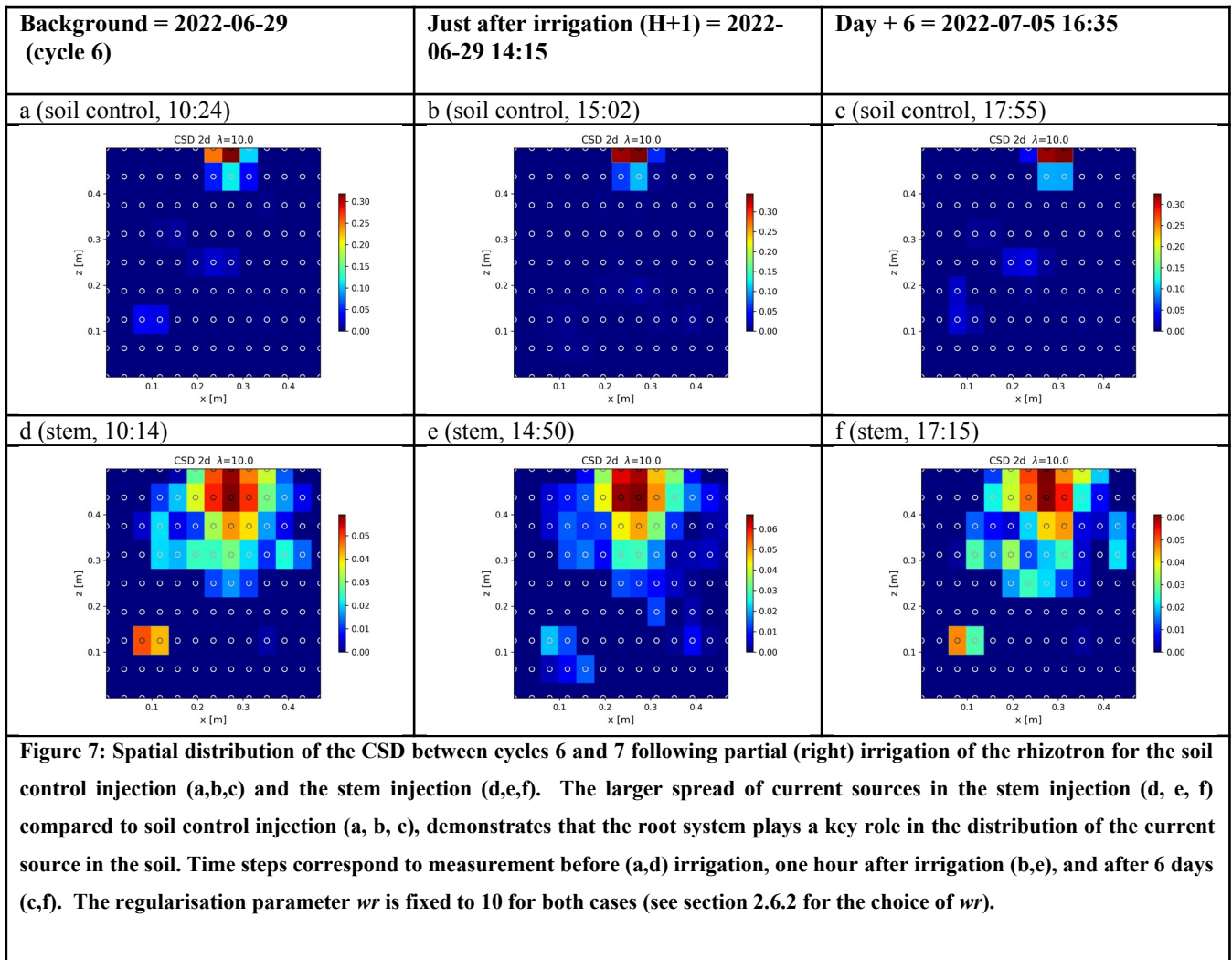
509

Figure 6: (a) Evolution of the quantity (in mL) of water input spatially distributed alternatively between left (green) and right (orange) during the PRD irrigation. (b) Evolution of the centre of mass (in the x direction) of the current density, while cross markers show the acquisition times. Cycle 6 to 7 windows were selected for the MALM time-lapse spatial analysis (Figure 7).

510

71

72



511

512

513

3.5. Correlations between soil parameters and estimated transpiration rates.

514

This section aims at drawing correlations between the soil parameters (ER, SWC, and CSD) and the

515

transpiration estimated from the rhizotron weight data. We do not account for the weight variations due to

516

the plant and root growth material (as this can be considered negligible relative to water dynamics). For

517

each node of the mesh, ER values are translated to SWC using Archie's law with the calibrated parameters

518

m and n (see Sect. 2.6.3). Averaging is performed on the mesh nodes falling within each side, with the

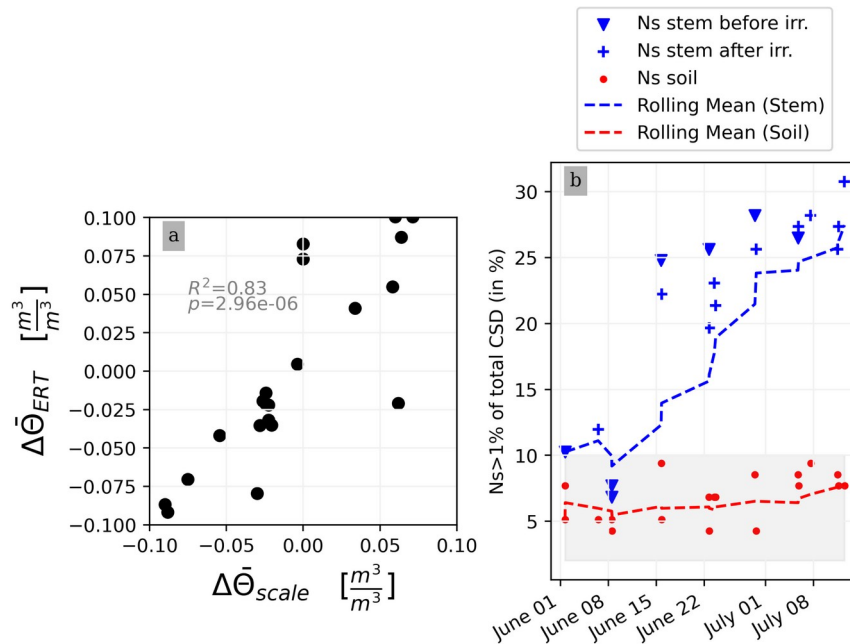
519

middle point being defined as half of the rhizotron width, equivalent to 0.25m. To simplify, we assume that

74

75

both porosity and fluid water conductivity are homogeneous in space and time (i.e no mixing between the tap water used for cycle 3 and the nutrient solution for all the other times). The maximum SWC observed after irrigation is about $0.42 \text{ m}^3/\text{m}^3$ (figure not shown). The minimum SWC of about $0.25 \text{ m}^3/\text{m}^3$ is repeatedly observed (see Fig. C1) just before each irrigation, meaning that the driest times are below field capacity conditions (estimated at $0.4 \text{ m}^3/\text{m}^3$). By examining the fluctuations in weight, one can calculate the corresponding changes in spatially averaged water content. Figure 8a illustrates a linear trend ($R^2=0.83$ and $p=2.96\text{e-}6$) between the inferred water content variations from the scale and those obtained from ERT (after Archie transformation). The most significant positive changes in averaged water content are attributable to the triggered irrigation, leading to a $\Delta\theta$ (change in water content) of -0.1 . Conversely, negative changes primarily result from transpiration, with a maximum value located at $+0.1$.



530

531 **Figure 8: (a) Changes in water content calculated from weight changes related to the changes in water content calculated from the**
 532 **ERT measurements. (b) relationship between the number of the current sources (Ns) carrying at least 1% of the total density**
 533 **(A.m-2) with respect to the time of the experiment. CSD results are obtained after inversion with a regularisation parameter wr of**
 534 **10. Cases of the stem before cycle 3 (grey), after cycle 3 (black) and the soil (blue) injections. All cycles are considered.**
 535
 536

537

538

539

540

541

542

543

544

Figure 8b shows the relationship between the variation of the percentage of the current sources carrying at least 1% of the total density (N_{s1}) used as an estimator for current density dispersion with respect to the datetime of the experiment. For the soil injection (red dots), N_{s1} is relatively constant between 5 to 10% of the total number of possible injection nodes (grey area). For the stem injections, N_{s1} increases over the course of the experiment. From June 1st to July 8th, the N_{s1} triple. There is no distinction between N_{s1} measured before (triangle point) and after (crossed points) irrigation.

545 4. Discussion

546

4.1. Validity of ERT and ECI in demonstrating the effects of the alternating irrigation scheme

547

548

549

550

551

552

553

554

555

556

557

558

559

560

Our first assumption was that the variations in ER (or in SWC inferred from the ER) are relevant as a proxy of root activity. Its validity has been checked against direct observation using the variations of weights measured from the scale data used as an indicator of plant transpiration. On average, in our experiment, the plant maintained high rates of transpiration to about 6 mm/day for each cycle except for the last cycle (number 9) where a decline was observed (Fig. 3). This range is in line with another rhizotron experiment where narrow-leaf lupin plants were grown: Garrigues et al. (2006) measured a mean rate of 3 mm/day. It is commonly found in the scientific literature that changes in ER are associated with root activity (e.g., Michot et al., 2003; Garré et al., 2011; Cassiani et al., 2015; Whalley et al., 2017). Here we had further confirmation of this, with a significant correlation between ER changes and gravimetric soil moisture changes (derived from the load cell) (Fig. 8). The leaf stomatal conductance and visual observation of plant above- and below-ground material growth were additional ancillary data to interpret the general state of the plant. Our observation is in line with the literature i.e. in general, low soil water content (SWC) can lead to drought stress in plants, which can result in decreased leaf stomatal conductance and less transpiration, and vice-versa.

80

81

561 A second assumption was that, when applying the alternative irrigation scheme, only one part of the root
562 system would be active and the current injected in the stem would only spread to the side where the root
563 system is irrigated. This assumption was not directly supported by the observations. Figures 6 and 7 show
564 that the influence of the irrigation pattern was negligible on the spatial distribution of the inverted CSD and
565 that the current distribution was not correlated with ER variations. It is true that active roots have higher
566 hydraulic conductivity but on the other hand, increased membrane permeability may encourage current
567 leakage into the soil. We nevertheless noticed that the CSD spatial distribution, while the rhizotron is
568 irrigated at its full length (cycles 0 to 3), was significantly different from the side irrigation cycles (Fig.
569 B4). Indeed, homogeneous irrigation without applying stress to the plant results in a very shallow current
570 leakage. Our observations potentially suggest that under conditions where soil electrical conductances are
571 high near the soil-root interface and even if there is good electrical contact between soil and roots, the
572 distribution of current source density might not be directly related to water uptake distributions. Further
573 research is needed to confirm this potential relationship.

574

575 **4.2. Effect of soil water content and transpiration demand**

576 Soil water content can affect the distribution of the current leakage by influencing the minimum resistance
577 pathways, i.e., whether roots and/or soil provide the minimum resistance to the current flow. Literature
578 reports that electrical capacitance method better estimates crop root traits under dry conditions (Gu et al.,
579 2021). In order to make a comparison with capacitance studies, we assumed that if the current distribution
580 remains unchanged (i.e. leaking into the same areas), there must be minimal changes in the electrical
581 capacitance. In this study, supposing no impact of the initial model, Fig. 8 shows that there is no apparent
582 effect of the soil water content on the current density distribution. Note that the soil water content
583 estimated is the bulk contribution of roots and soil, as only one pedophysical relationship was used, while
584 recent studies tend to show that mixed soil-root pedophysical relationships are preferable (e.g. Rao et al.,
585 2018). Moreover, considering small-scale variations around individual root segments in terms of water

586 content and soil hydraulic properties becomes crucial for a comprehensive understanding of the system..
587 This is clearly limiting our ability to interpret the independent contribution of the soil and the roots, yet this
588 does not limit our ability to identify zones where water availability leads to root water uptake.

589

590 Based on Fig. 2 and 8b, the association between water stress and leaf development, along with
591 transpiration demand, is expected to be more prominent (and increasing during the course of the
592 experiment rather than the specific time points before and after irrigation). Indeed the fluctuations in water
593 content during various cycles, with or without stress, exhibited remarkable similarity. Both stressed and
594 non-stressed cycles experienced a drop in water content to similar low levels. Consequently, water content
595 does not appear to account for the variability in water stress. Instead, it is the increased transpiration
596 demand over time that seems to play a more significant role in driving the observed changes. At high
597 transpiration demand, stress may occur at higher soil water contents because the soil becomes limiting for
598 the root water uptake. The changes in water potential and water content in the vicinity of the soil-root
599 interface can potentially impact the electrical conductivity of the immediate soil surrounding the roots.
600 Consequently, as the experiment progressed, lower electrical conductances in the soil around the roots,
601 potentially led to a restriction in the flow of current between the root system and the soil. This, in turn, may
602 have resulted in a more uniform distribution of the electrical current source along the entire length of the
603 root system.

604

605

606 **4.3. Possible mitigation of the PRD effect**

607 In general, a PRD irrigation experiment must comply with two criteria: (1) a minimum soil water content
608 to trigger a physiological response and, (2) a distinction between a wet and a dry side (Stoll, 2000). In our
609 experiment, the first criterion was met, but not the second. This provides an interesting piece of evidence,
610 leading to the following considerations:.

- 611 (1) According to McAdam et al. (2016) and Collins et al. (2009), ABA is triggered even by mild soil
612 stress values. Consequently, plants adapt the hydraulic conductivity of their roots as well as that
613 of the soil in their vicinity through exudates (Carminati and Javaux, 2020). Results from previous
614 irrigation experiments using PRD or DI have shown that changes in stomatal conductance and
615 shoot growth are some of the major components affected (Düring et al., 1996). In our experiment,
616 the shoot growth fitted with the conventional leaf area and growth models, except at the end of
617 the experiment when signs of water stress were visible on some leaves. The magnitude of the
618 shoot growth is correlated with the number of roots. Drought may cause more inhibition of shoot
619 growth than of root growth (Sharp and Davies, 1989). Although the root system was already well
620 developed it is not possible to exclude its development as a factor influencing the CSD
621 distribution.
- 622 (2) The spatiotemporal analysis of the ER showed that the water changes were not limited to root
623 effects. Water redistribution from dry to wet in the soil and from shoot to dry roots (Smart et al.,
624 2005, Lovisolo et al., 2016) may have occurred (Fig. A1 to A11). Additionally, even not visible
625 from the screening face, capillary rise may have taken place due to the presence of a saturated
626 zone at the bottom of the rhizotron. Due to the fact that water drained on both sides, RWU was
627 not only vertically distributed but also horizontally. The range of water content varied
628 significantly with a minimum SWC of about $0.25 \text{ m}^3/\text{m}^3$, repeatedly observed just before each
629 irrigation meaning that the driest times are below field capacity conditions (estimated at 0.4
630 m^3/m^3). Drying half of the root system resulted in a reduction of the stomatal conductance (based
631 on the mean of the distribution) of the order $5 \text{ mmol m}^{-2}\text{s}^{-1}$ after a 1 week cycle. Given the stress
632 applied, the ER changes highlighted that root played a major role in the wine plant survival and
633 evidenced strategies of adaptation. Indeed, the plant was able to adjust its water uptake and
634 redistribution zones depending on the water availability, from all places, not only from the
635 alternate irrigated areas.

636 (3) Finally, in order to know if the PRD conditions are met it would have been important not to
637 neglect the different states of root growth, and root renewal (because of renewal and decay) with
638 respect to the geophysical data. Nevertheless, this would have required opening and scanning the
639 rhizotron with conventional methods. Finally, we did not make a distinction between the hours of
640 the day although the changes observed for the irrigation are rapid, usually at the hourly scale, and
641 could be similar for RWU.

642

643

644 4.4. Performance of the acquisition protocol and the processing

645

646

647

648

649

650

651

652

653

654

655

656

657

658

659

660

We discuss here how the quality of the recovered current density models by evaluating the performance of the protocol and the processing. First, it is important to note that although the ERT data quality was good (very few reciprocals were rejected, see Table A1), the inverted model was not perfect and this ultimately has an impact also on the ECI forward model. The algorithm has undergone testing in a rhizotron experiment and has demonstrated the ability to differentiate punctual sources, even when their current contribution is as low as 5% of the total current (Peruzzo et al., 2020). The CSD resolution, of course, matches the electrode interspace (in this case 5cm) and the smoothness constraint does not impact the simulation of point source reconstruction. We adopted an inversion without any prior information to recover the current density. Only model smoothing was applied by weighting the model data by an optimal factor of 10 inferred from an L-curve analysis. Similar to the ERT inversion, the CSD problem is also ill-posed. In this case, the 4-electrodes setup ensures that the current will flow through the plant after injection, regardless of the contact resistance. However, the accuracy of the measured data may be impacted by contact resistance, as errors in the measured resistance will negatively affect the quality of ERT and CSD inversions. The impact is more pronounced on CSD, as it is dependent on ERT. Lastly, because the box is relatively small and no-current-flow boundary conditions (Neumann) are imposed, we

661 may expect an effect due to the position of the return electrode where the current is attracted due to the
662 strongest gradient nearby (Mary et al., 2019b).

663

664

665 **4.5. Outlook**

666 In order to strictly correlate PRD effects with geophysical measurements, one should consider a physical
667 barrier to separate the two sides of the rhizotron to a split-roots configuration. Another option is to increase
668 the lateral size to prevent redistribution or to use a very percolating material such as glass beads, gravels or
669 coarse sands. This should be carefully considered, as the rhizotron must also be an environment where
670 plant growth is possible under “natural” conditions, and for this some water retention capacity is needed
671 for the soil. A larger drainage capacity would simplify the interpretation as no-water redistribution from
672 one side to the other can occur. Although considering a barrier is technically possible, it would require a
673 more complex inversion scheme of the ERT and ECI considering that no electrical current can flow from
674 side to side. One could also consider increasing the measurement frequency to catch processes at an
675 hourly scale and comparing day/night measurements, particularly those associated with water
676 redistribution from the stem back to the roots at night when transpiration is reduced and its effect on the
677 water status of the roots. As we have seen that most of the water changes occurred in the day consecutive
678 to the irrigation, catching rapid changes of ER would help drive a conclusion on how much ECI is
679 connected to the active root zone. Finally, in order to draw robust statistical conclusions, the experiments
680 should be replicated for multiple plant samples.

681 **5. Conclusion**

682 The study aimed at understanding the current path in the root system and active root zones using geoelectrical imaging,
683 considering soil water content and irrigation regimes. Electrical Resistivity Tomography (ERT) is sensitive to both irrigation
684 and RWU processes. The ECI model uses a physical approach to measure current density after stem stimulation. The CSD

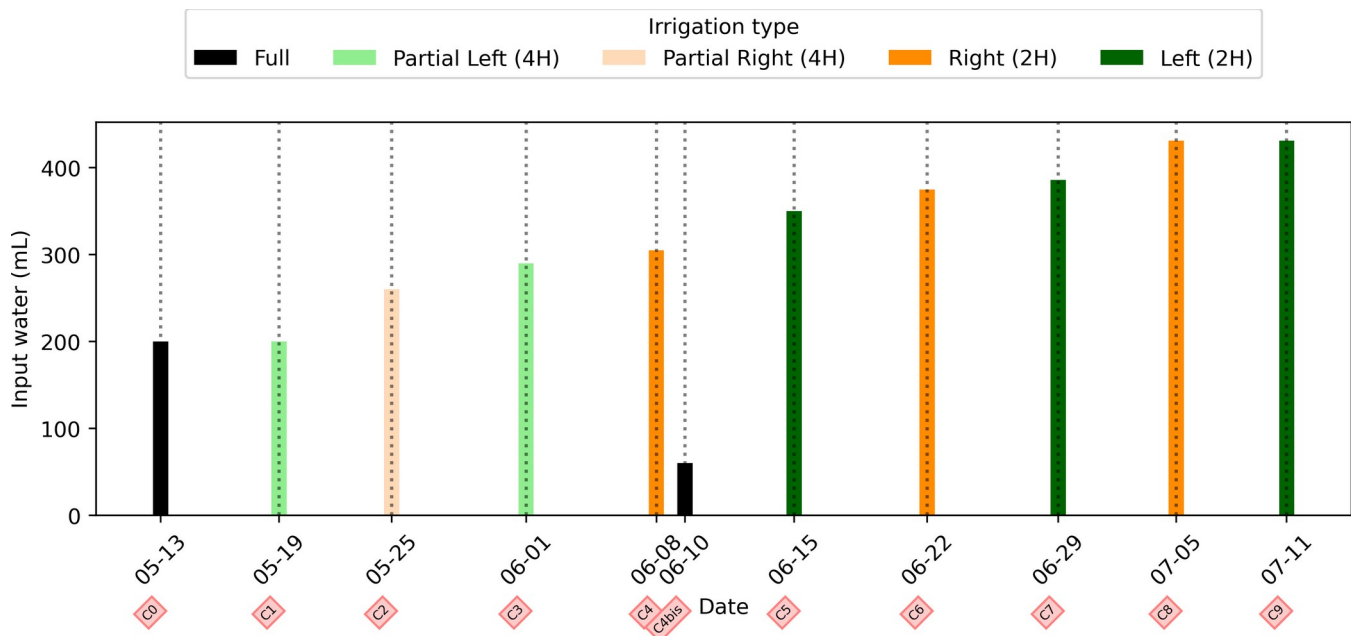
685 was very different from the control soil injection to the stem injection but nevertheless did not correlate with PRD cycles as
 686 originally expected. We demonstrate that under mild stress conditions, it is practically impossible to spatially distinguish the
 687 PRD effects using the ECI. We only evidenced that the Current Source Density distribution varied during the course of the
 688 experiment considering evaporative demand but without any significant relationship to the Soil Water Content changes . A
 689 few aspects of the experiment would gain to be more closely studied such as the water redistribution that possibly also
 690 affects current distribution. In the future, we expect to improve our understanding by coupling the geophysical experiment
 691 with an unsaturated soil-plant-atmosphere model.

692 6. Appendices

693 Appendix A: Time-lapse ERT inversion results

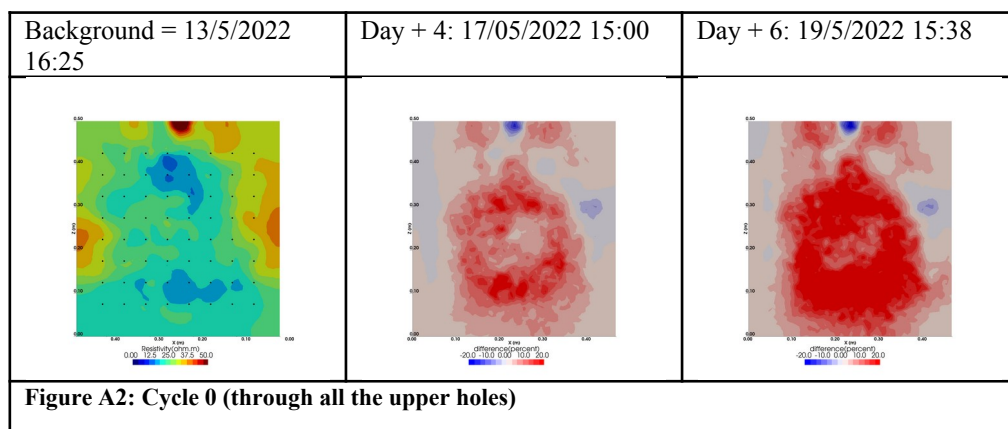
694 As we selected only one cycle in the manuscript, we report here further details about the time-lapse ERT inversion results for
 695 all the cycles. The inversion procedure is equivalent to the one described in Sect. 2.6.1 of the manuscript (Data processing -
 696 Analysis of the ERT data). All time-lapse inversion models are plotted with a unique scale ranging from -20 to 20% of
 697 changes.

698

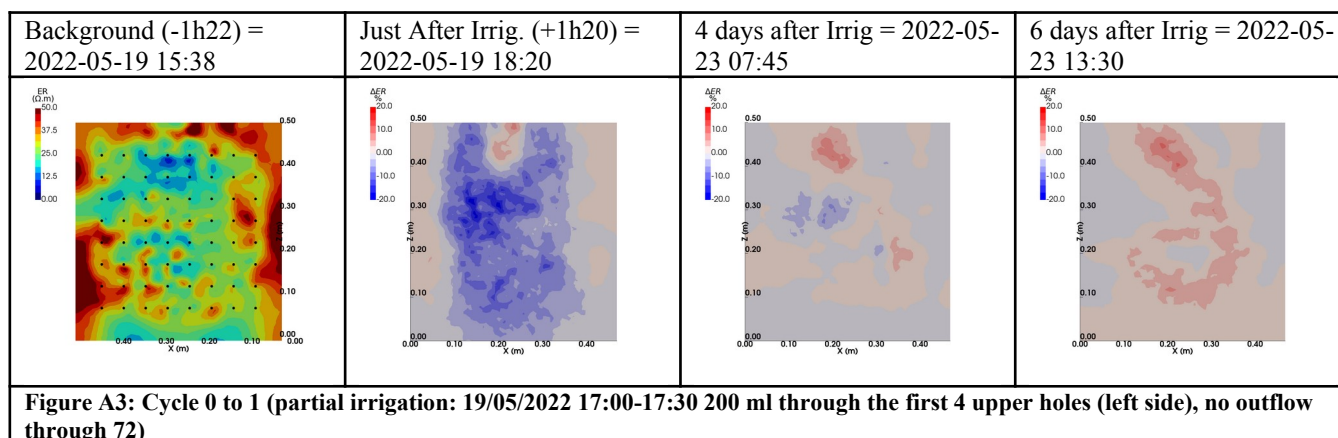


100
700
701
702
703
704
705
706
707
708
709

Figure A1: Evolution of the quantity (in mL) of water input spatially distributed with an alternate between left (green) and right (orange) during the PRD irrigation. The black bars hold for full-width irrigation (over all the holes, see fig. 1 manuscript), light green and orange bars hold for irrigation over the 4 sides of holes, and dark green/orange for 2 holes irrigation.



710
711



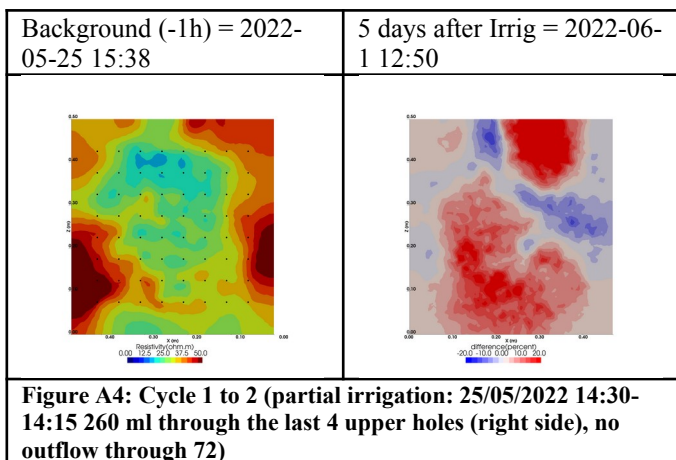
712
713

101
102

103

714

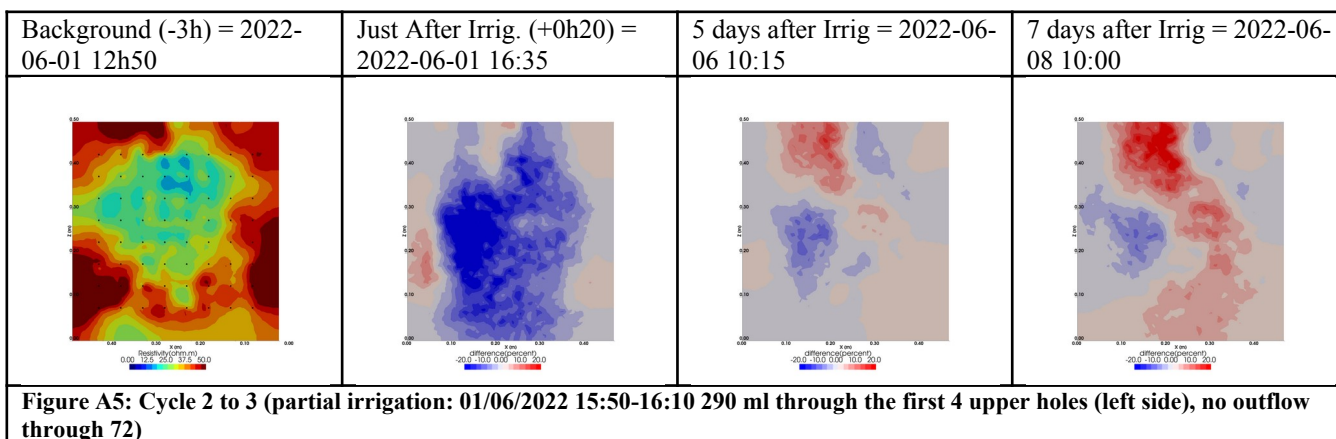
715



716

717

718



719

720

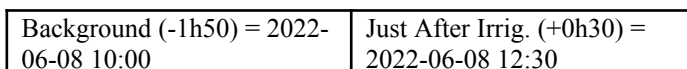
721

722

723

724

725



104

105

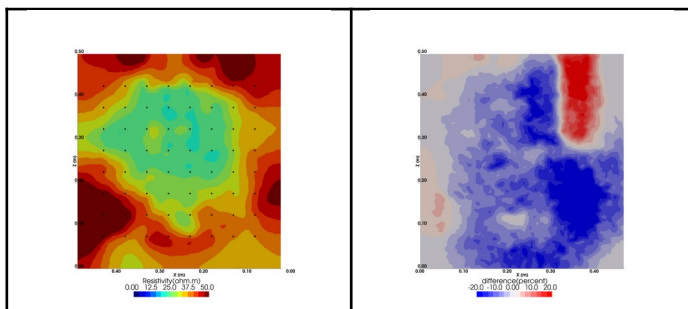
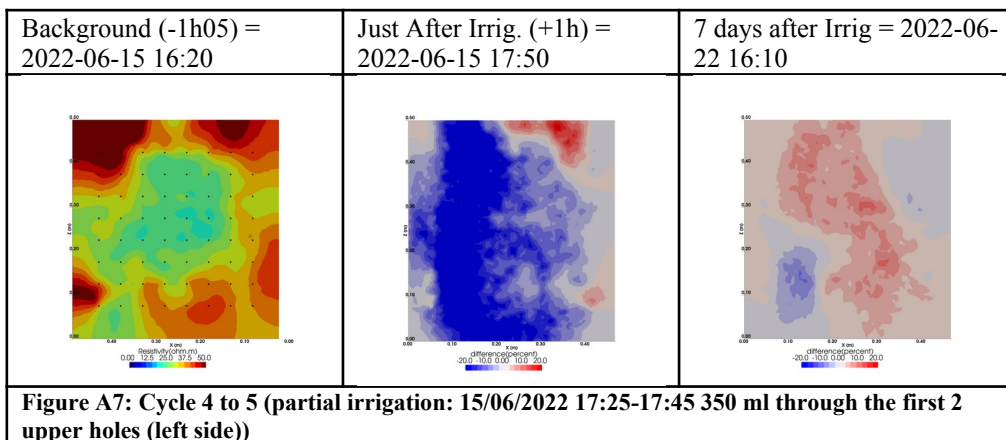


Figure A6: Cycle 3 to 4 (partial irrigation: 08/06/2022 11:50-12:00 305 ml through the last 2 upper holes (right side))

726



727

728

729

730

731

732

733

734

735

736

Background (-0h35) = 2022-06-22 16:10	Just After Irrig. (+0h30) = 2022-06-22 17h21	17h after Irrig = 2022-06-23 10:55	1 day after Irrig = 2022-06-23 15:20	6 days after Irrig = 2022-06-29 9:30

107

108

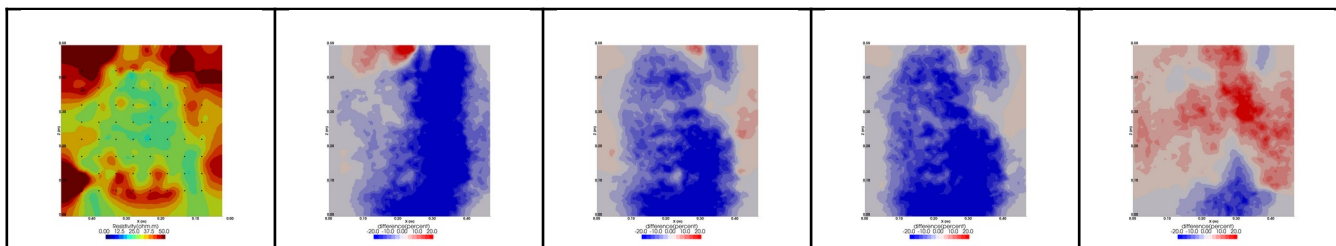


Figure A8: Cycles 5 and 6 time-lapse inversion (partial right side irrigation 22/06/2022 16:45-17:00, 375 ml)

737

738

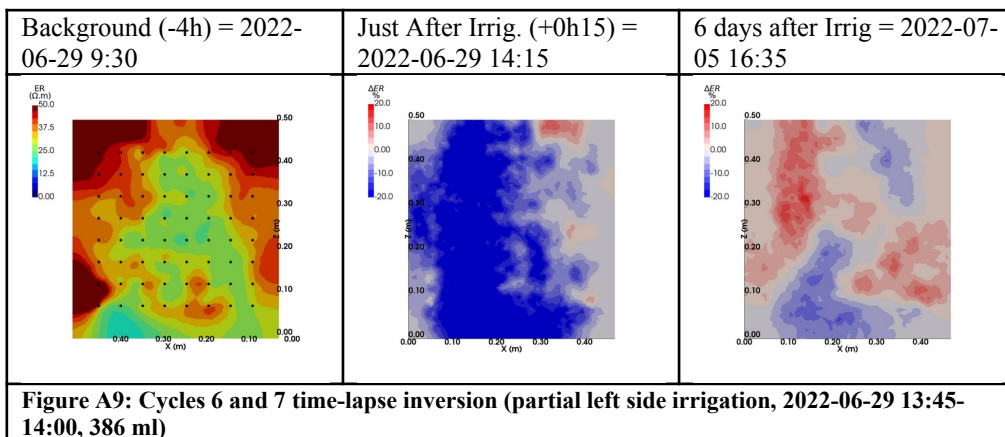
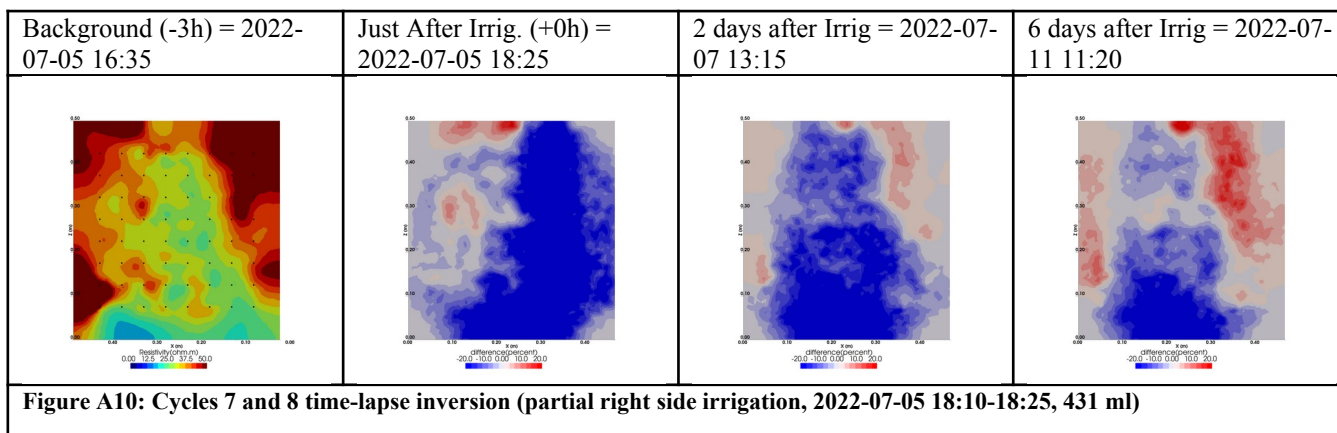


Figure A9: Cycles 6 and 7 time-lapse inversion (partial left side irrigation, 2022-06-29 13:45-14:00, 386 ml)

739

740

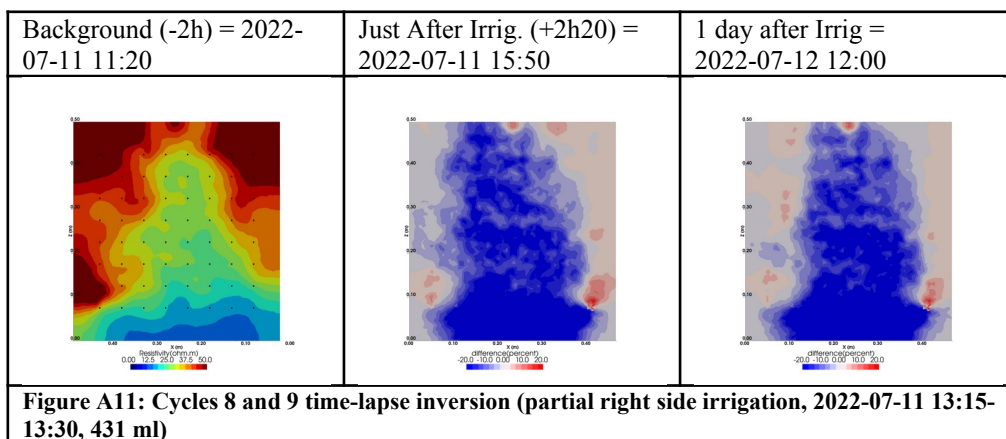
741



742

743

744



745

746

747

748

749

750

751

752

753

Date	RMS (%)	# measurements read (over 2484)
2022-06-01 12:50:00	1.36	2048
2022-06-01 16:35:00	1.15	1920
2022-06-06 10:15:00	1.53	2268

113

114

2022-06-08 10:00:00	1.41	2230
2022-06-08 12:30:00	1.16	2028
2022-06-15 16:20:00	1.08	2137
2022-06-15 17:50:00	1.47	1493
2022-06-22 16:10:00	1.38	2109
2022-06-22 17:21:00	1.14	1372
2022-06-23 10:55:00	1.48	2229
2022-06-23 15:20:00	1.38	2268
2022-06-29 09:30:00	1.27	2075
2022-06-29 14:15:00	2.04	2027
2022-07-05 16:35:00	1.7	2067
2022-07-05 18:25:00	1.85	980
2022-07-07 13:15:00	1.98	2225
2022-07-11 11:20:00	2.5	2093
2022-07-11 15:50:00	2.72	2238
2022-07-12 12:00:00	2.68	2255

754 **Table A1: Table summarising the final RMS and the number of data used for each individual inversion**

755

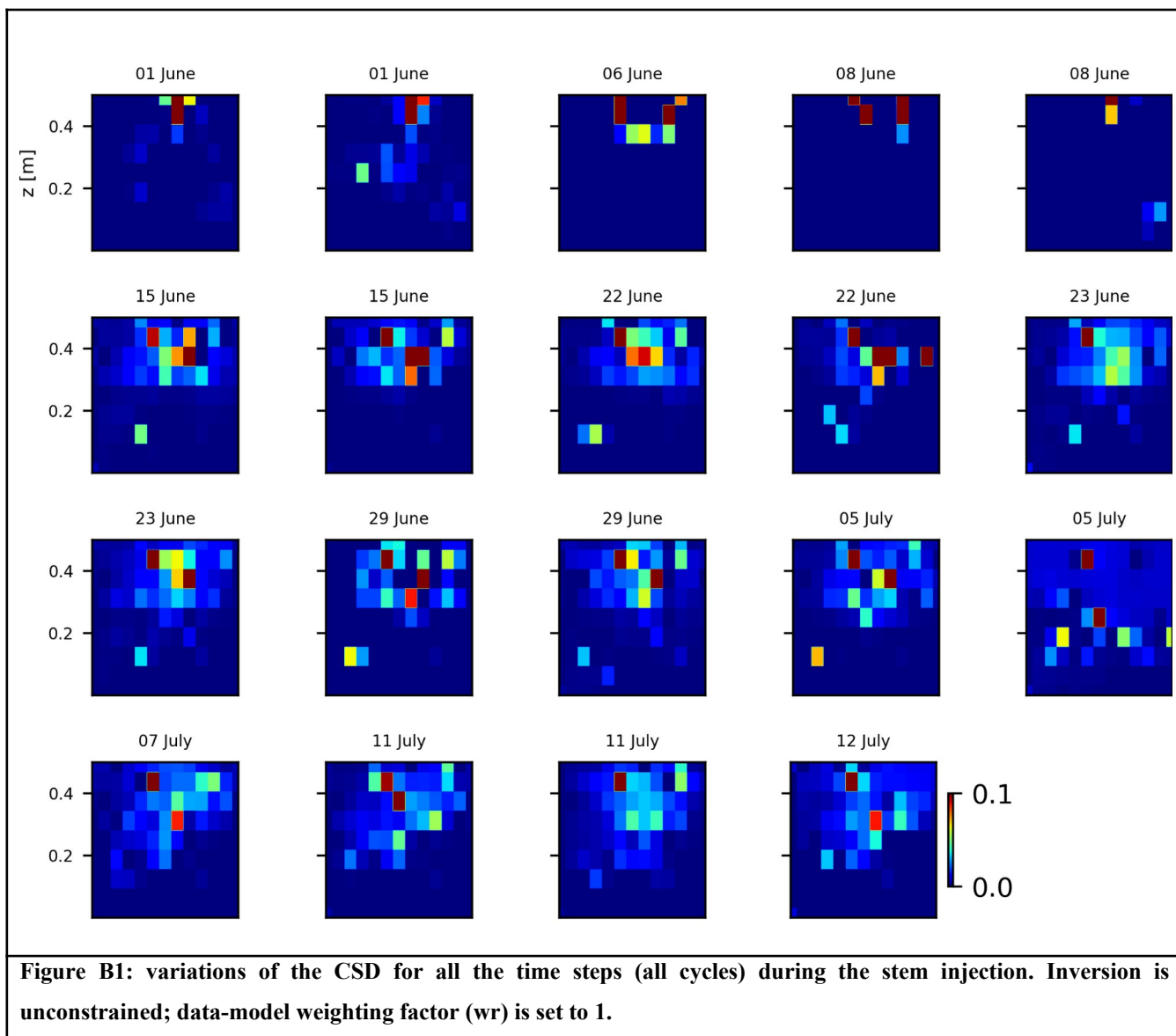
756

757

758 **Appendix B: Inversion of current density (CSD)**

759

760 As we selected only one cycle in the manuscript, we report here further details about the time-lapse CSD inversion results
761 for all the cycles. The inversion procedure is equivalent to the one described in Sect. 2.6.2 of the manuscript (Data
762 processing - Analysis of current density) and we invite the reader to refer to Peruzzo et al. (2020) for a full description of the
763 algorithm. Furthermore, we extend the analysis showing the effect of the model regularisation (smoothing). Figures B1 and
764 B2 show the current density evolution with the time respectively for the stem and the soil injection with a regularisation
765 parameter of 1. The same is for Figures B3 and B4 with a regularisation of 10.



766

767

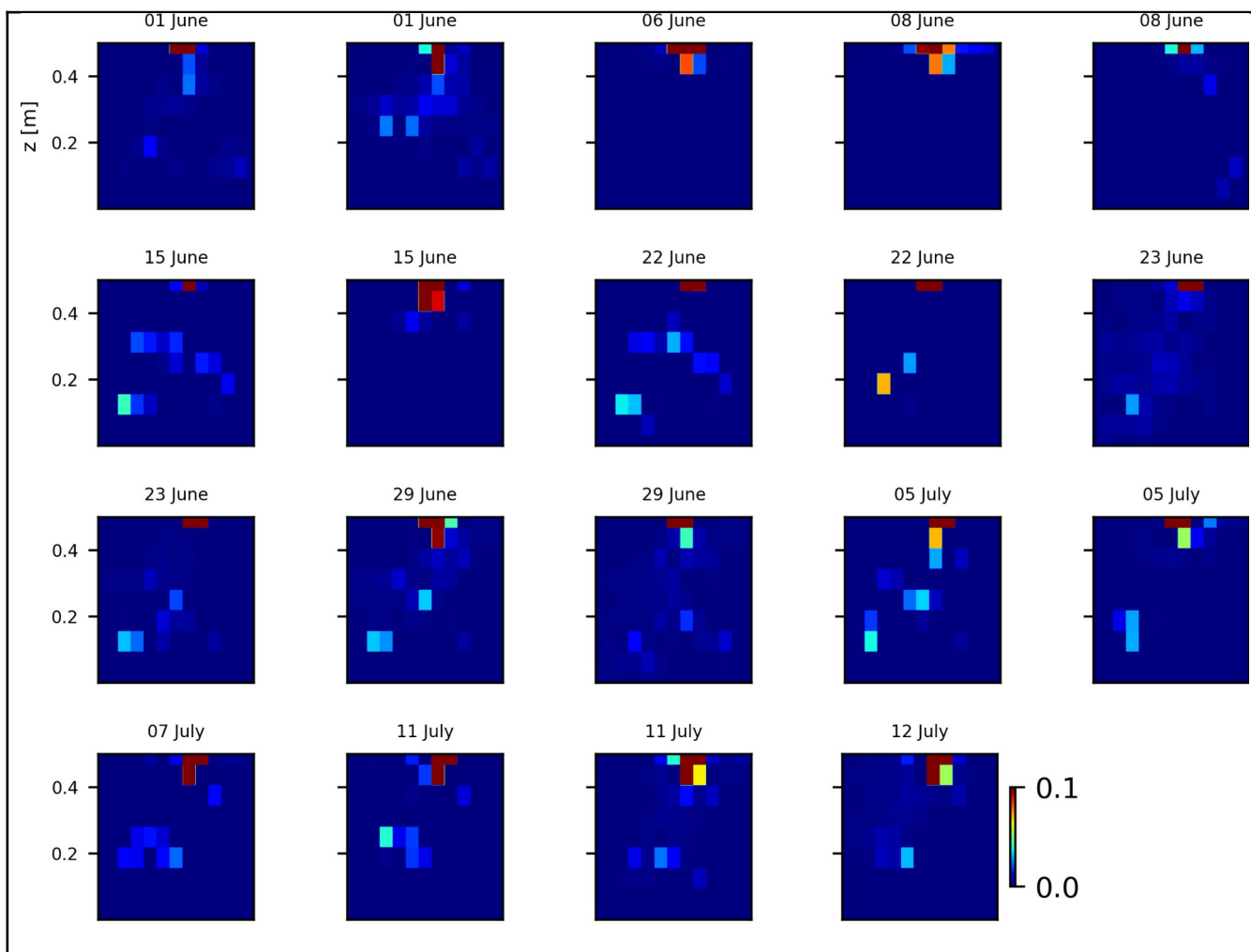


Figure B2: variations of the CSD for all the time steps (all cycles) during the soil control injection. Inversion is unconstrained; data-model weighting factor (w_r) is set to 1.

768

769

770

771

772

122

123

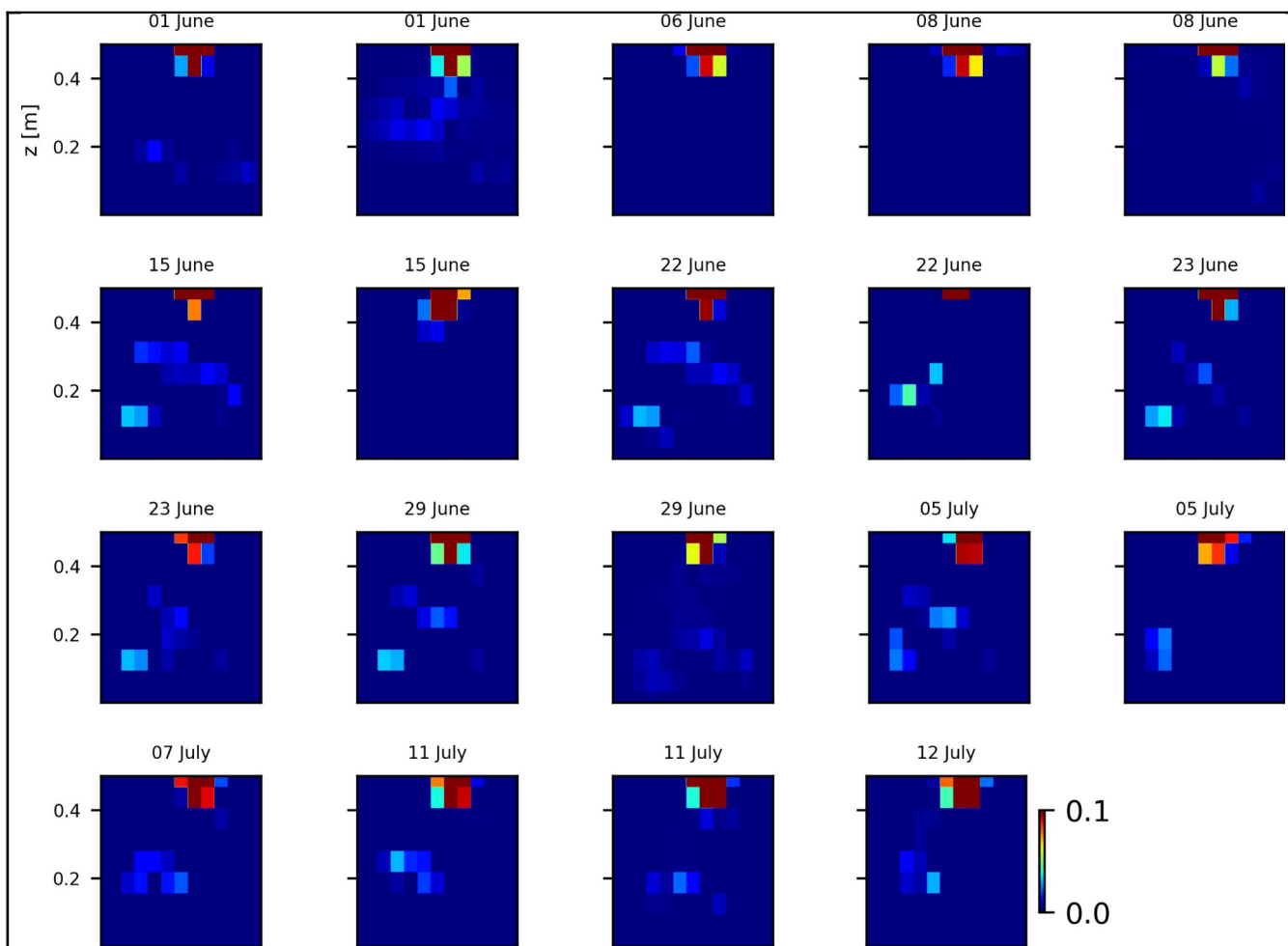


Figure B3: variations of the CSD for all the time steps (all cycles) during the soil control injection. Inversion is unconstrained; data-model weighting factor (w_r) is set to 10.

773

774

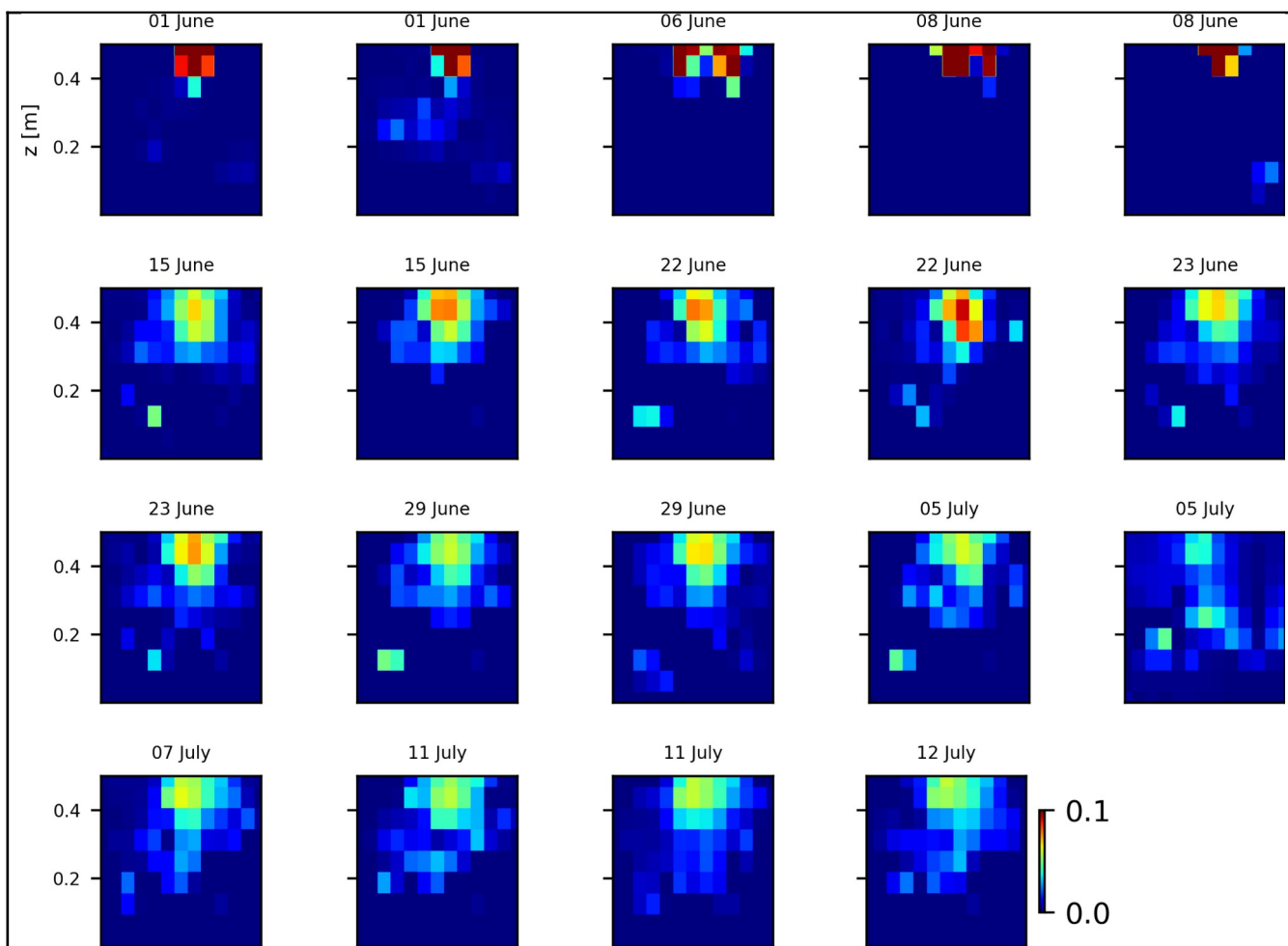


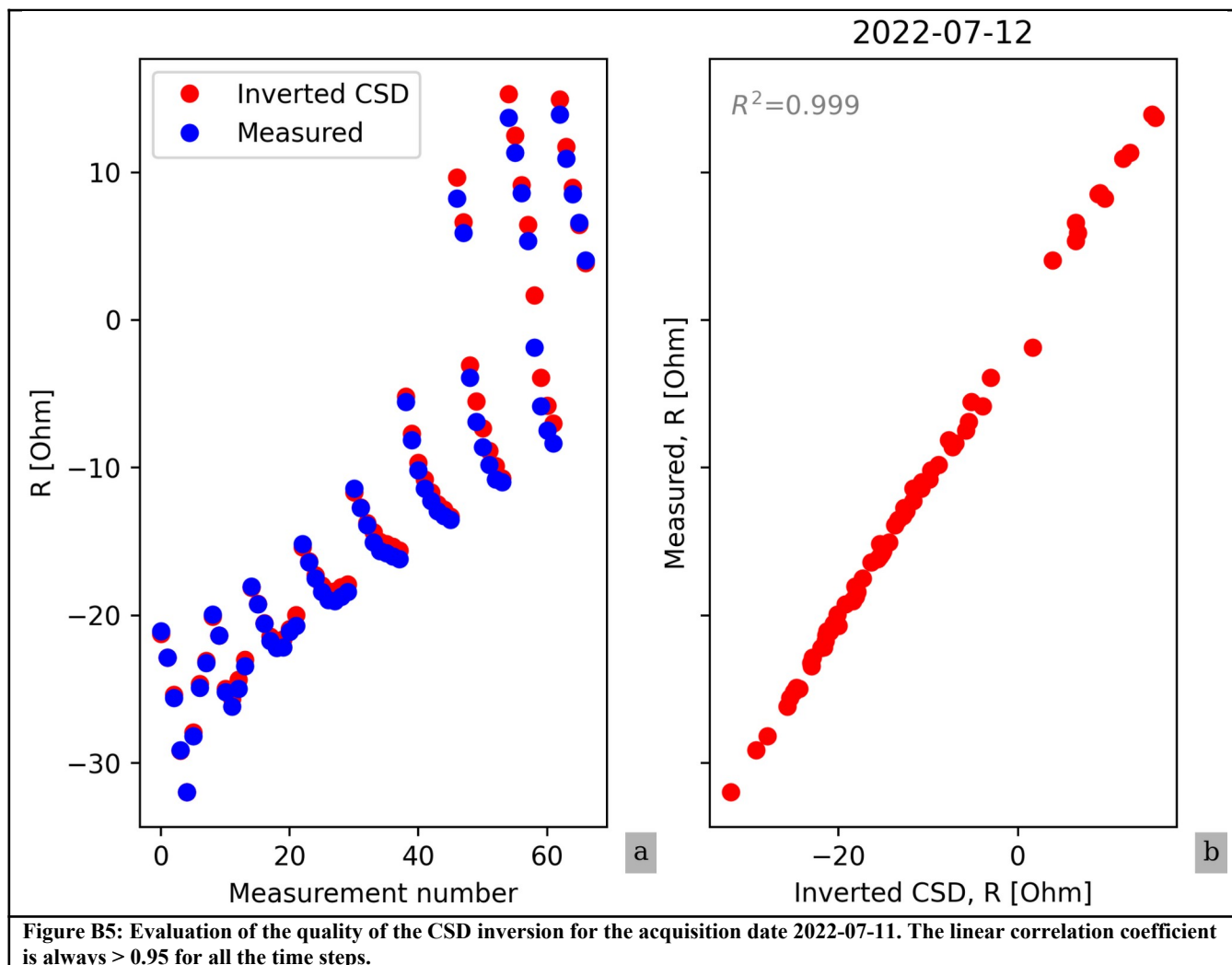
Figure B4: variations of the CSD for all the time steps (all cycles) during the stem injection. Inversion is unconstrained; data-model weighting factor (w_r) is set to 10.

775

776

777

778



779

780

133

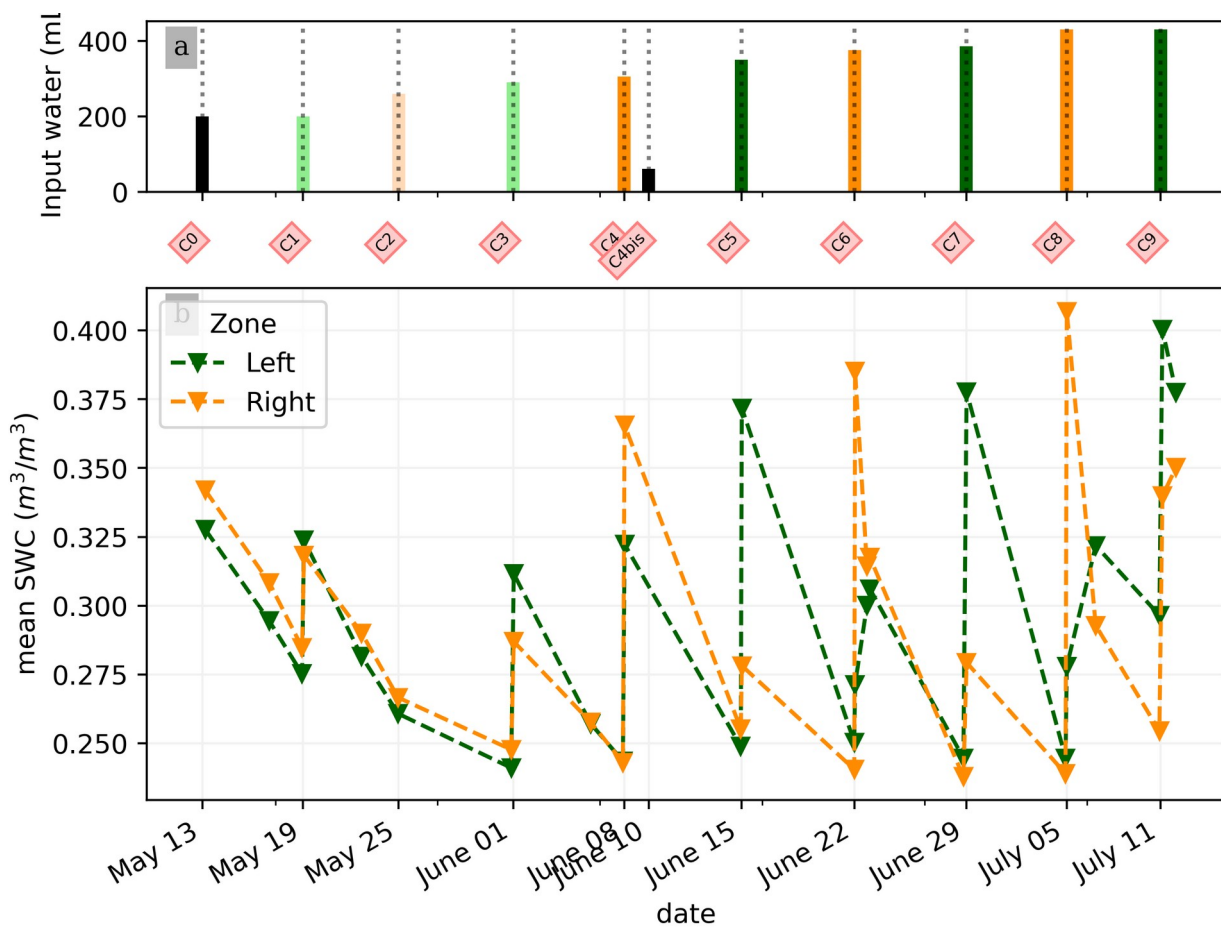
781

782 **Appendix C: Soil Water Content converted variations**

783

784

785



134

135

787 **Figure C1: (a) Evolution of the quantity (in mL) of water input spatially distributed with an alternate between left**
788 **(green) and right (orange) during the PRD irrigation. The black bars hold for full-width irrigation (over all the**
789 **holes, see fig. 1 manuscript), light green and orange bars hold for irrigation over the 4 sides of holes, and dark**
790 **green/orange for 2 holes irrigation. (b) Evolution of the mean SWC (m³/m³) average on each side, markers show**
791 **the acquisition time.**

792 7. Data availability

793 Codes and data to reproduce figures articles are available in the Zenodo data repository (link to come after decision).

794

795

796 *Competing interests*

797 The authors declare that they have no conflict of interest.

798

799 *Author contribution*

800 BM, VI, LP, FM, BR, CC, YW and GB designed the experiments, and BM, VI, BR and FM carried them out. BM, LP, GB ,
801 CC developed the model code and performed the simulations. BM prepared the manuscript with contributions from all co-
802 authors for writing – review & editing.

803

804

805 *Acknowledgments*

806 Benjamin Mary acknowledges the financial support from European Union's Horizon 2020 research and innovation
807 programme under a Marie Skłodowska-Curie grant agreement (grant no. 842922).

808

809 References

- 810 1. Anonymous Reviewer: Comment on bg-2023-58, <https://doi.org/10.5194/bg-2023-58-RC2>, n.d.
- 811 2. Archie, G. E.: The Electrical Resistivity Log as an Aid in Determining Some Reservoir Characteristics, Trans.
812 AIME, 146, 54–62, <https://doi.org/10.2118/942054-G>, 1942.
- 813 3. Binley, A.: 11.08 - Tools and Techniques: Electrical Methods, in: Treatise on Geophysics (Second Edition), edited
814 by: Schubert, G., Elsevier, Oxford, 233–259, <https://doi.org/10.1016/B978-0-444-53802-4.00192-5>, 2015.

- 815 4. Binley, A. and Slater, L.: Resistivity and induced polarization: theory and applications to the near-surface earth,
816 Cambridge University Press, Cambridge, UK ; New York, NY, 2020.
- 817 5. Blanchy, G., Saneiyani, S., Boyd, J., McLachlan, P., and Binley, A.: ResIPy, an intuitive open source software for
818 complex geoelectrical inversion/modeling, *Comput. Geosci.*, 137, 104423,
819 <https://doi.org/10.1016/j.cageo.2020.104423>, 2020.
- 820 6. Carminati, A. and Javaux, M.: Soil Rather Than Xylem Vulnerability Controls Stomatal Response to Drought,
821 *Trends Plant Sci.*, 25, 868–880, <https://doi.org/10.1016/j.tplants.2020.04.003>, 2020.
- 822 7. Cassiani, G., Boaga, J., Vanella, D., Perri, M. T., and Consoli, S.: Monitoring and modelling of soil–plant
823 interactions: the joint use of ERT, sap flow and eddy covariance data to characterize the volume of an orange tree
824 root zone, *Hydrol. Earth Syst. Sci.*, 19, 2213–2225, <https://doi.org/10.5194/hess-19-2213-2015>, 2015.
- 825 8. Cassiani, G., Boaga, J., Rossi, M., Putti, M., Fadda, G., Majone, B., and Bellin, A.: Soil–plant interaction monitoring:
826 Small scale example of an apple orchard in Trentino, North-Eastern Italy, *Science of The Total Environment*, 543,
827 851–861, <https://doi.org/10.1016/j.scitotenv.2015.03.113>, 2016.
- 828 9. Collins, M., Fuentes, S., and Barlow, E.: Partial rootzone drying and deficit irrigation increase stomatal sensitivity
829 to vapour pressure deficit in anisohydric grapevines, *Funct Plant Biol*, 37, 129–138, 2009.
- 830 10. Consoli, S., Stagno, F., Vanella, D., Boaga, J., Cassiani, G., and Rocuzzo, G.: Partial root-zone drying irrigation in
831 orange orchards: Effects on water use and crop production characteristics, *European Journal of Agronomy*, 82, 190–
832 202, <https://doi.org/10.1016/j.eja.2016.11.001>, 2017.
- 833 11. Cseresnyés, I., Vozáry, E., Kabos, S., and Rajkai, K.: Influence of substrate type and properties on root electrical
834 capacitance, *Int. Agrophysics*, 34, 95–101, <https://doi.org/10.31545/intagr/112147>, 2020.
- 835 12. Dalton, F. N.: In-situ root extent measurements by electrical capacitance methods, *Plant Soil*, 173, 157–165,
836 <https://doi.org/10.1007/BF00155527>, 1995.
- 837 13. Dietrich, S., Carrera, J., Weinzettel, P., and Sierra, L.: Estimation of Specific Yield and its Variability by Electrical
838 Resistivity Tomography, *Water Resour. Res.*, 54, 8653–8673, <https://doi.org/10.1029/2018WR022938>, 2018.

- 839 14. Doussan, C. and Garrigues, E.: Measuring and Imaging the Soil-root-water System with a Light Transmission 2D
840 Technique, *Bio-Protocol*, 9, <https://doi.org/10.21769/BioProtoc.3190>, 2019.
- 841 15. Düring, H., Dry, P. R., Botting, D. G., and Loveys, B.: Effects of partial root-zone drying on grapevine vigour,
842 yield, composition of fruit and use of water, in: *Proceedings of the Ninth Australian Wine Industry Technical*
843 *Conference: Adelaide, South Australia, 16-19 July 1995*, 1996, págs. 128-131, *Proceedings of the Ninth Australian*
844 *Wine Industry Technical Conference: Adelaide, South Australia, 16-19 July 1995*, 128–131, 1996.
- 845 16. Ehosioke, S., Nguyen, F., Rao, S., Kremer, T., Placencia-Gomez, E., Huisman, J. A., Kemna, A., Javaux, M., and
846 Garré, S.: Sensing the electrical properties of roots: A review, *Vadose Zone J.*, 19, e20082,
847 <https://doi.org/10.1002/vzj2.20082>, 2020.
- 848 17. Elsner, E. A. and Jubb, G. L.: Leaf Area Estimation of Concord Grape Leaves from Simple Linear Measurements,
849 *Am. J. Enol. Vitic.*, 39, 95–97, 1988.
- 850 18. Garré, S., Javaux, M., Vanderborght, J., Pagès, L., and Vereecken, H.: Three-dimensional electrical resistivity
851 tomography to monitor root zone water dynamics, *Vadose Zone Journal*, 10, 412–424,
852 <https://doi.org/10.2136/vzj2010.0079>, 2011.
- 853 19. Garré, S., Hyndman, D., Mary, B., and Werban, U.: Geophysics conquering new territories: The rise of
854 “agrogeophysics,” *Vadose Zone J.*, 20, e20115, <https://doi.org/10.1002/vzj2.20115>, 2021.
- 855 20. Garrigues, E., Doussan, C., and Pierret, A.: Water Uptake by Plant Roots: I – Formation and Propagation of a Water
856 Extraction Front in Mature Root Systems as Evidenced by 2D Light Transmission Imaging, *Plant Soil*, 283, 83–98,
857 <https://doi.org/10.1007/s11104-004-7903-0>, 2006.
- 858 21. Geuzaine, C. and Remacle, J.-F.: Gmsh: A 3-D finite element mesh generator with built-in pre- and post-processing
859 facilities, *Int. J. Numer. Methods Eng.*, 79, 1309–1331, <https://doi.org/10.1002/nme.2579>, 2009.
- 860 22. Gibert, D., Le Mouél, J.-L., Lambs, L., Nicollin, F., and Perrier, F.: Sap flow and daily electric potential variations
861 in a tree trunk, *Plant Science*, 171, 572–584, <https://doi.org/10.1016/j.plantsci.2006.06.012>, 2006.

- 862 23. Gimenez, C., Gallardo, M., and Thompson, R. B.: PLANT–WATER RELATIONS, in: Encyclopedia of Soils in the
863 Environment, edited by: Hillel, D., Elsevier, Oxford, 231–238, <https://doi.org/10.1016/B0-12-348530-4/00459-8>,
864 2005.
- 865 24. Gu, H., Liu, L., Butnor, J., Sun, H., Zhang, X., Li, C., and Liu, X.: Electrical capacitance estimates crop root traits
866 best under dry conditions—a case study in cotton (*Gossypium hirsutum* L.), *Plant Soil*, 467, 1–19,
867 <https://doi.org/10.1007/s11104-021-05094-6>, 2021.
- 868 25. Hoagland, D. R. and Arnon, D. I. (1950). The water culture method for growing plants without soil. California
869 Agric Exp Stn Circ 347: 1-32.
- 870 26. Jackisch, C., Knoblauch, S., Blume, T., Zehe, E., and Hassler, S. K.: Estimates of tree root water uptake from soil
871 moisture profile dynamics, *Biogeosciences*, 17, 5787–5808, <https://doi.org/10.5194/bg-17-5787-2020>, 2020.
- 872 27. Kamarajan, C., Pandey, A. K., Chorlian, D. B., and Porjesz, B.: The use of current source density as
873 electrophysiological correlates in neuropsychiatric disorders: a review of human studies, *Int. J. Psychophysiol. Off.*
874 *J. Int. Organ. Psychophysiol.*, 97, 310–322, <https://doi.org/10.1016/j.ijpsycho.2014.10.013>, 2015.
- 875 28. Liu, Y., Li, D., Qian, J., Di, B., Zhang, G., and Ren, Z.: Electrical impedance spectroscopy (EIS) in plant roots
876 research: a review, *Plant Methods*, 17, <https://doi.org/10.1186/s13007-021-00817-3>, 2021.
- 877 29. Lovisolo, C., Lavoie-Lamoureux, A., Tramontini, S., and Ferrandino, A.: Grapevine adaptations to water stress:
878 new perspectives about soil/plant interactions, *Theor. Exp. Plant Physiol.*, 28, 53–66,
879 <https://doi.org/10.1007/s40626-016-0057-7>, 2016.
- 880 30. Malavasi, U. C., Davis, A. S., and Malavasi, M. de M.: Lignin in Woody Plants under Water Stress: A Review,
881 *Floresta E Ambiente*, 23, 589–597, <https://doi.org/10.1590/2179-8087.143715>, 2016.
- 882 31. Michot, D., Benderitter, Y., Dorigny, A., Nicoullaud, B., King, D., and Tabbagh, A.: Spatial and temporal
883 monitoring of soil water content with an irrigated corn crop cover using surface electrical resistivity tomography:
884 Soil Water Study Using Electrical Resistivity, *Water Resour. Res.*, 39, <https://doi.org/10.1029/2002WR001581>,
885 2003.
- 886 32. Mancuso, S. (Ed.): *Measuring roots: an updated approach*, Springer, Heidelberg ; New York, 382 pp., 2012.

- 887 33. Martin-Vertedor, A. I. and Dodd, I. C.: Root-to-shoot signalling when soil moisture is heterogeneous: increasing the
888 proportion of root biomass in drying soil inhibits leaf growth and increases leaf abscisic acid concentration: Root
889 distribution and non-hydraulic signalling, *Plant Cell Environ.*, 34, 1164–1175, [https://doi.org/10.1111/j.1365-](https://doi.org/10.1111/j.1365-3040.2011.02315.x)
890 3040.2011.02315.x, 2011.
- 891 34. Mary, B., Peruzzo, L., Boaga, J., Schmutz, M., Wu, Y., Hubbard, S. S., and Cassiani, G.: Small-scale
892 characterization of vine plant root water uptake via 3-D electrical resistivity tomography and mise-à-la-masse
893 method, *Hydrol. Earth Syst. Sci.*, 22, 5427–5444, <https://doi.org/10.5194/hess-22-5427-2018>, 2018.
- 894 35. Mary, B., Vanella, D., Consoli, S., and Cassiani, G.: Assessing the extent of citrus trees root apparatus under deficit
895 irrigation via multi-method geo-electrical imaging, *Sci. Rep.*, 9, 9913, <https://doi.org/10.1038/s41598-019-46107-w>,
896 2019a.
- 897 36. Mary, B., Rao, S., Javaux, M., and Cassiani, G.: Tree root system mise-à-la-masse (MALM) forward modelling
898 with explicit representation of root structure., in: *Geophysical Research Abstracts*, 2019b.
- 899 37. McAdam, S. A. M., Sussmilch, F. C., and Brodribb, T. J.: Stomatal responses to vapour pressure deficit are
900 regulated by high speed gene expression in angiosperms, *Plant Cell Environ.*, 39, 485–491,
901 <https://doi.org/10.1111/pce.12633>, 2016.
- 902 38. Parsekian, A. D., Claes, N., Singha, K., Minsley, B. J., Carr, B., Voytek, E., Harmon, R., Kass, A., Carey, A.,
903 Thayer, D., and Flinchum, B.: Comparing Measurement Response and Inverted Results of Electrical Resistivity
904 Tomography Instruments, *J. Environ. Eng. Geophys.*, 22, 249–266, <https://doi.org/10.2113/JEEG22.3.249>, 2017.
- 905 39. Peruzzo, L., Chou, C., Wu, Y., Schmutz, M., Mary, B., Wagner, F. M., Petrov, P., Newman, G., Blancaflor, E. B.,
906 Liu, X., Ma, X., and Hubbard, S.: Imaging of plant current pathways for non-invasive root Phenotyping using a
907 newly developed electrical current source density approach, *Plant Soil*, 450, 567–584,
908 <https://doi.org/10.1007/s11104-020-04529-w>, 2020.
- 909 40. Peruzzo, L., Liu, X., Chou, C., Blancaflor, E. B., Zhao, H., Ma, X.-F., Mary, B., Iván, V., Weigand, M., and Wu,
910 Y.: Three-channel electrical impedance spectroscopy for field-scale root phenotyping, *Plant Phenome J.*, 4, e20021,
911 <https://doi.org/10.1002/ppj2.20021>, 2021.

- 912 41. Postic, F. and Doussan, C.: Benchmarking electrical methods for rapid estimation of root biomass, *Plant Methods*,
913 12, 33, <https://doi.org/10.1186/s13007-016-0133-7>, 2016.
- 914 42. Rao, S., Meunier, F., Ehosioke, S., Lesparre, N., Kemna, A., Nguyen, F., Garré, S., and Javaux, M.: A mechanistic
915 model for electrical conduction in soil–root continuum: a virtual rhizotron study, *Biogeochemistry: Land*,
916 <https://doi.org/10.5194/bg-2018-280>, 2018.
- 917 43. Sartoni, R., Zegada-Lizarazu, W., and Monti, A.: A new compartmentalised rhizotron system for root phenotyping,
918 *Ital. J. Agron.*, 10, 53, <https://doi.org/10.4081/ija.2015.645>, 2015.
- 919 44. Sharp, R. E. and Davies, W. J.: Regulation of growth and development of plants growing with a restricted supply of
920 water, *Semin. Ser. - Soc. Exp. Biol.*, 1989.
- 921 45. Smart, D. R., Carlisle, E., Goebel, M., and Nunez, B. A.: Transverse hydraulic redistribution by a grapevine, *Plant*
922 *Cell Environ*, 28, 157–166, <https://doi.org/10.1111/j.1365-3040.2004.01254.x>, 2005.
- 923 46. Song, C., Shen, W., Du, L., Wen, J., Lin, J., and Li, R.: Development and chemical characterization of Casparian
924 strips in the roots of Chinese fir (*Cunninghamia lanceolata*), *Trees*, 33, 827–836, [https://doi.org/10.1007/s00468-](https://doi.org/10.1007/s00468-019-01820-x)
925 [019-01820-x](https://doi.org/10.1007/s00468-019-01820-x), 2019.
- 926 47. Stoll, M.: Effects of partial rootzone drying on grapevine physiology and fruit quality, 2000.
- 927 48. Stoll, M., Loveys, B., and Dry, P.: Hormonal changes induced by partial rootzone drying of irrigated grapevine,
928 *Journal of Experimental Botany*, 51, 1627–1634, <https://doi.org/10.1093/jexbot/51.350.1627>, 2000.
- 929 49. Taylor, H. M., Upchurch, D. R., and McMichael, B. L.: Applications and limitations of rhizotrons and
930 minirhizotrons for root studies, *Plant Soil*, 129, 29–35, <https://doi.org/10.1007/BF00011688>, 1990.
- 931 50. Tsialtas, J. T., Koundouras, S., and Zioziou, E.: Leaf area estimation by simple measurements and evaluation of leaf
932 area prediction models in Cabernet-Sauvignon grapevine leaves, *Photosynthetica*, 46, 452–456,
933 <https://doi.org/10.1007/s11099-008-0077-x>, 2008.
- 934 51. Tsukanov, K. and Schwartz, N.: Relationship between wheat root properties and its electrical signature using the
935 spectral induced polarization method, *Vadose zone j.*, 19, <https://doi.org/10.1002/vzj2.20014>, 2020.

- 936 52. Tsukanov, K. and Schwartz, N.: Modeling Plant Roots Spectral Induced Polarization Signature, *Geophys. Res.*
937 *Lett.*, 48, e2020GL090184, <https://doi.org/10.1029/2020GL090184>, 2021.
- 938 53. Uhlemann, S., Wilkinson, P. B., Maurer, H., Wagner, F. M., Johnson, T. C., and Chambers, J. E.: Optimized survey
939 design for electrical resistivity tomography: combined optimization of measurement configuration and electrode
940 placement, *Geophys. J. Int.*, 214, 108–121, <https://doi.org/10.1093/gji/ggy128>, 2018.
- 941 54. Urban, J., Bequet, R., and Mainiero, R.: Assessing the applicability of the earth impedance method for in situ
942 studies of tree root systems, *J. Exp. Bot.*, 62, 1857–1869, <https://doi.org/10.1093/jxb/erq370>, 2011.
- 943 55. Vanella D., G. Cassiani, L. Busato, J. Boaga, S. Barbagallo, A. Binley, S. Consoli, 2018, Use of small scale
944 electrical resistivity tomography to identify soil-root interactions during deficit irrigation, *Journal of Hydrology*,
945 556, 310-324, doi: 10.1016/j.jhydrol.2017.11.025.
- 946 56. Virtanen, P., Gommers, R., Oliphant, T. E., Haberland, M., Reddy, T., Cournapeau, D., Burovski, E., Peterson, P.,
947 Weckesser, W., Bright, J., van der Walt, S. J., Brett, M., Wilson, J., Millman, K. J., Mayorov, N., Nelson, A. R. J.,
948 Jones, E., Kern, R., Larson, E., Carey, C. J., Polat, İ., Feng, Y., Moore, E. W., VanderPlas, J., Laxalde, D., Perktold,
949 J., Cimrman, R., Henriksen, I., Quintero, E. A., Harris, C. R., Archibald, A. M., Ribeiro, A. H., Pedregosa, F., and
950 van Mulbregt, P.: SciPy 1.0: fundamental algorithms for scientific computing in Python, *Nat. Methods*, 17, 261–
951 272, <https://doi.org/10.1038/s41592-019-0686-2>, 2020.
- 952 57. Voytek, E. B., Barnard, H. R., Jougnot, D., and Singha, K.: Transpiration- and precipitation-induced subsurface
953 water flow observed using the self-potential method, *Hydrol. Process.*, <https://doi.org/10.1002/hyp.13453>, 2019.
- 954 58. Whalley, W. R., Binley, A., Watts, C. W., Shanahan, P., Dodd, I. C., Ober, E. S., Ashton, R. W., Webster, C. P.,
955 White, R. P., and Hawkesford, M. J.: Methods to estimate changes in soil water for phenotyping root activity in the
956 field, *Plant Soil*, 415, 407–422, <https://doi.org/10.1007/s11104-016-3161-1>, 2017.
- 957 59. Weigand, M.: Monitoring Structural And Physiological Properties Of Crop Roots Using Spectral Electrical
958 Impedance Tomography, University of Bonn, 2017.
- 959 60. Weigand, M. and Kemna, A.: Imaging and functional characterization of crop root systems using spectroscopic
960 electrical impedance measurements, *Plant Soil*, 435, 201–224, <https://doi.org/10.1007/s11104-018-3867-3>, 2019.

- 961 61. Yan, J., Bogie, N. A., and Ghezzehei, T. A.: Root uptake under mismatched distributions of water and nutrients in
962 the root zone, *Biogeosciences*, 17, 6377–6392, <https://doi.org/10.5194/bg-17-6377-2020>, 2020.